

New Research Proposal to Jefferson Lab PAC 44

## Deeply virtual Compton scattering on the neutron with a longitudinally polarized deuteron target

S. Niccolai<sup>1,2</sup>, G. Charles, R. Dupré, M. Guidal,  
D. Marchand, C. Munoz Camacho, E. Voutier  
*Institut de Physique Nucléaire d'Orsay, 91406 Orsay, France*

A. Biselli<sup>1</sup>  
*Fairfield University, Fairfield Connecticut 06824*

C. Keith<sup>1</sup>, H. Avakian, V. Burkert, F.X. Girod, L. Elouadrhiri,  
V. Kubarovsky, K. Park, P. Rossi, S. Stepanyan, M. Ungaro  
*Thomas Jefferson National Laboratory, Newport News, VA 23606*

S. Pisano<sup>1</sup>, V. Lucherini, M. Mirazita  
*INFN, Laboratori Nazionali di Frascati, 00044 Frascati, Italy*

D. Sokhan<sup>1</sup>, B. McKinnon, G. Murdoch  
*University of Glasgow, Glasgow, Scotland*

M. Battaglieri, A. Celentano, R. De Vita, E. Fanchini, M. Osipenko, M. Ripani, M. Taiuti  
*Istituto Nazionale di Fisica Nucleare, Sezione di Genova and  
Dipartimento di Fisica, Università di Genova, Genova, Italy 16146*

D. Crabb, D. Day, D. Keller  
*University of Virginia, Charlottesville, VA 22904*

I. Balossino, L. Barion, G. Ciullo, M. Contalbrigo, P. Lenisa,  
A. Movsyan, L. Pappalardo, M. Turisini  
*INFN, Istituto Nazionale di Fisica Nucleare, Sezione di Ferrara, Ferrara, Italy 44122*

A. D'Angelo, L. Lanza, A. Rizzo, I. Zonta  
*Università di Roma Tor Vergata and INFN Roma Tor Vergata, Roma, Italy 00133*

V. Bellini, F. Mammoliti, G. Russo, C.M. Sutura  
*Istituto Nazionale di Fisica Nucleare, Sezione di Catania, Catania, Italy 95123*

J. Ball, M. Defurne, M. Garçon, H. Moutarde, S. Procureur, F. Sabatié

---

<sup>1</sup>co-spokesperson

<sup>2</sup>contact person, email: silvia@jlab.org

*CEA, Centre de Saclay, Irfu/Service de Physique Nucléaire, 91191 Gif-sur-Yvette, France*

W.R. Armstrong, K. Hafidi, M. Hattawy  
*Argonne National Laboratory, Argonne, IL 60439*

K. Griffioen  
*College of William and Mary, Williamsburg, VA 23187*

K. Adhikari, L. El Fassi  
*Mississippi State University, MS 39762*

K. Slifer, E. Long, T. Badman, L. Hammed, S. Li, D. Ruth,  
S. Santiesteban, R. Zielinski  
*University of New Hampshire, Durham, NH 03824*

I. Skorodumina  
*University of South Carolina, Columbia, SC 29208*

G. Fetodov  
*Skobeltsyn Institute of Nuclear Physics, Lomonosov Moscow State, Russia*

A. Filippi  
*INFN, Istituto Nazionale di Fisica Nucleare, Sezione di Torino, Torino, Italy 10125*

## **A CLAS Collaboration proposal**

## Abstract

Measurements of Deeply Virtual Compton Scattering on the neutron (nDVCS) are necessary for a complete description of nucleon structure in terms of Generalized Parton Distributions (GPDs). Combining DVCS results from both proton and neutron targets will permit the flavor decomposition of the GPDs. An experimental program of nDVCS has commenced at JLab with the already-approved experiment E12-11-003 to measure beam-spin asymmetries over a wide kinematic range using the CLAS12 detector. Here we propose to extend this program by measuring, for the first time, both target-spin and double-spin asymmetries for nDVCS using a longitudinally polarized deuteron target inside CLAS12. The measurements will be made detecting the electron and the photon in the forward part of CLAS12, and the recoil neutron in the recently completed Central Neutron Detector, thus assuring the exclusivity of the nDVCS reaction ( $ed \rightarrow e'n\gamma(p)$ ). By fitting these results together with the beam-spin asymmetries measured by E12-11-003 at the same kinematic points, an extraction of several neutron Compton Form Factors (CFFs) can be made.  $\Im(\mathcal{E}_n)$  and  $\Im(\mathcal{H}_n)$  will be especially well determined thanks to their dominance in the beam- and target-spin asymmetries, respectively. Quark-flavor separation of the GPDs then becomes possible through a combination of the extracted neutron CFFs with those obtained from proton DVCS. In order to provide a mapping of the nDVCS single and double target-spin asymmetries over the available 4-dimensional ( $Q^2$ ,  $x_B$ ,  $-t$ ,  $\phi$ ) phase space, and thus achieve an acceptable extraction of the neutron CFFs accessible from these observables, we request 50 days of running on a ND<sub>3</sub> polarized target, plus 10 days of calibration and ancillary runs, with the maximum available beam energy of 11 GeV. This beam time coincides with the one already approved for the ND<sub>3</sub> portion of run group C of CLAS12.

# Contents

<b>1</b>	<b>Introduction: Generalized Parton Distributions and DVCS</b>	<b>3</b>
<b>2</b>	<b>Physics motivation: neutron GPDs and flavor separation</b>	<b>5</b>
<b>3</b>	<b>DVCS spin observables</b>	<b>5</b>
3.1	Target-spin asymmetry . . . . .	7
3.2	Double-spin asymmetry . . . . .	7
<b>4</b>	<b>Extraction of CFFs from fits to DVCS observables</b>	<b>8</b>
<b>5</b>	<b>Experimental situation</b>	<b>8</b>
<b>6</b>	<b>Experimental setup</b>	<b>10</b>
6.1	Polarized target . . . . .	10
6.1.1	Luminosity . . . . .	12
6.1.2	Polarization measurement . . . . .	12
6.1.3	Overhead for target operation . . . . .	13
6.2	Central Neutron Detector . . . . .	16
6.3	Simulation and reconstruction . . . . .	18
6.3.1	Efficiency . . . . .	20
6.3.2	Angular and momentum resolutions . . . . .	20
6.3.3	Particle Identification . . . . .	22
<b>7</b>	<b>nDVCS at CLAS12: kinematics and acceptances</b>	<b>24</b>
<b>8</b>	<b>Measurement of the asymmetries</b>	<b>24</b>
8.1	Event selection and exclusivity cuts . . . . .	25
<b>9</b>	<b>Neutral pion background</b>	<b>30</b>
<b>10</b>	<b>Dilution factor</b>	<b>32</b>
<b>11</b>	<b>Accidentals in the CND</b>	<b>34</b>
<b>12</b>	<b>Projected results</b>	<b>36</b>
<b>13</b>	<b>Extraction of Compton Form Factors</b>	<b>37</b>
<b>14</b>	<b>Flavor separation of CFFs</b>	<b>37</b>
<b>15</b>	<b>Systematic uncertainties</b>	<b>48</b>
<b>16</b>	<b>Beam-time request</b>	<b>51</b>
<b>17</b>	<b>Conclusions</b>	<b>52</b>
<b>A</b>	<b>Appendix: Count rates and acceptances</b>	<b>52</b>

# 1 Introduction: Generalized Parton Distributions and DVCS

It is well known that the fundamental particles which form hadronic matter are the quarks and the gluons, whose interactions are described by the Lagrangian of quantum chromodynamics (QCD). However, exact QCD-based calculations cannot yet be performed to explain all the properties of hadrons in terms of their constituents. Therefore, phenomenological functions need to be used to connect experimental observables with the inner dynamics of the constituents of the nucleon, the partons. Typical examples of such functions include form factors, parton densities, and distribution amplitudes. Generalized Parton Distributions (GPDs) are nowadays the object of an intense effort of research, in the perspective of understanding nucleon structure. The GPDs describe the correlations between the longitudinal momentum and transverse spatial position of the partons inside the nucleon. They give access to the contribution of the orbital momentum of the quarks to the nucleon, and they are sensitive to the correlated  $q - \bar{q}$  components. The original articles and general reviews on GPDs and details of the formalism can be found in Refs. [1]-[7].

The nucleon GPDs are the structure functions which are accessed in the measurement of the exclusive leptonproduction of a photon (DVCS, which stands for deeply virtual Compton scattering) or of a meson on the nucleon, at sufficiently large  $Q^2$ , where  $Q^2$  is the virtuality of the photon emitted by the initial lepton, for the reaction to happen at the quark level. Figure 1 illustrates the leading process for DVCS, also called the “handbag diagram”. At leading-order QCD and at leading twist, considering only quark-helicity conserving quantities and the quark sector, the process is described by four GPDs,  $H^q, \tilde{H}^q, E^q, \tilde{E}^q$ , one for each quark flavor  $q$ , that account for the possible combinations of relative orientations of nucleon spin and quark helicity between the initial and final state.  $H$  and  $E$  do not depend on the quark helicity and are therefore called unpolarized GPDs while  $\tilde{H}$  and  $\tilde{E}$  depend on the quark helicity and are called polarized GPDs.  $H$  and  $\tilde{H}$  conserve the spin of the nucleon, whereas  $E$  and  $\tilde{E}$  correspond to a nucleon-spin flip.

The GPDs depend upon three variables,  $x$ ,  $\xi$  and  $t$ :  $x + \xi$  and  $x - \xi$  are the longitudinal momentum fractions of the struck quark before and after scattering, respectively, and  $t$  is the squared four-momentum transfer between the initial and final nucleon (see caption of Fig. 1 for the definitions of these variables). The transverse component of  $t$  is the Fourier-conjugate variable of the transverse position of the struck parton in the nucleon. Among the three variables,  $x$ ,  $\xi$  and  $t$ , which appear in the DVCS formalism, only  $\xi$  and  $t$  are experimentally accessible in these reactions.

The DVCS amplitude is proportional to combinations of integrals over  $x$  of the form:

$$\int_{-1}^1 dx F(\mp x, \xi, t) \left[ \frac{1}{x - \xi + i\epsilon} \pm \frac{1}{x + \xi - i\epsilon} \right] \quad (1)$$

where  $F$  represents one of the four GPDs. The top combination of the plus and minus signs applies to the quark-helicity independent, or unpolarized, GPDs ( $H, E$ ), and the bottom combination of signs applies to the quark-helicity dependent, or polarized, GPDs ( $\tilde{H}, \tilde{E}$ ). Each of these 4 integrals, which are called Compton Form Factors (CFFs), can be decomposed into

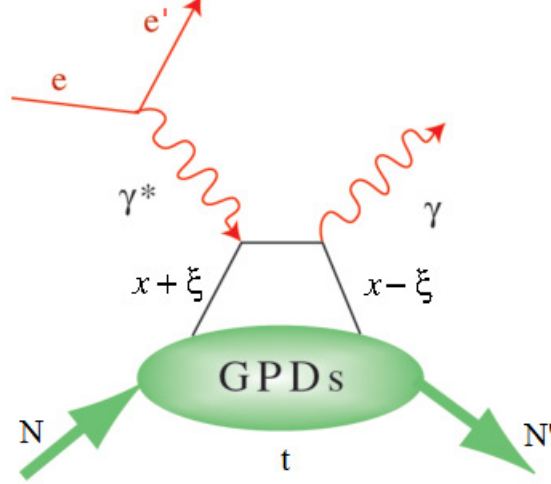


Figure 1: The handbag diagram for the DVCS process on the nucleon  $eN \rightarrow e'N'\gamma'$ . Here  $x+\xi$  and  $x-\xi$  are the longitudinal momentum fractions of the struck quark before and after scattering, respectively, and  $t = (N - N')^2$  is the squared four-momentum transfer between the initial and final nucleons (or equivalently between the two photons). In the Bjorken limit, i.e. for  $Q^2 \rightarrow \infty$  and  $\nu \rightarrow \infty$  so that  $x_B = \frac{Q^2}{2M\nu}$  is finite,  $\xi$  is proportional to the Bjorken scaling variable  $x_B$  ( $\xi \simeq \frac{x_B}{2-x_B}$ , where  $x_B = \frac{Q^2}{2M\nu}$ ,  $M$  is the nucleon mass and  $\nu$  is the difference between the energies of the initial and final electron in the lab frame). A crossed diagram also exists, but it is not shown here.

their real and imaginary parts, as

$$\Re \mathcal{F}(\xi, t) = \mathcal{P} \int_{-1}^1 dx \left[ \frac{1}{x-\xi} \mp \frac{1}{x+\xi} \right] F(x, \xi, t) \quad (2)$$

$$\Im \mathcal{F}(\xi, t) = -\pi [F(\xi, \xi, t) \mp F(-\xi, \xi, t)], \quad (3)$$

where  $\mathcal{P}$  is Cauchy's principal value integral and the sign convention is the same as in Eq. 1. The information that can be extracted from the experimental data at a given  $(\xi, t)$  point depends on the observable involved.  $\Re \mathcal{F}$  is accessed primarily measuring observables which are sensitive to the real part of the DVCS amplitude, such as double-spin asymmetries, beam-charge asymmetries or unpolarized cross sections.  $\Im \mathcal{F}$  can be obtained measuring observables which are mainly sensitive to the imaginary part of the DVCS amplitude, such as single-spin asymmetries or cross-section differences. However, knowing the CFFs does not define the GPDs uniquely. A model input is necessary to deconvolute their  $x$  dependence.

The DVCS process is accompanied by the Bethe-Heitler (BH) process, in which the final-state real photon is radiated by the incoming or scattered electron and not by the nucleon itself. The BH process, which is not sensitive to the GPDs, is experimentally indistinguishable from DVCS and interferes with it at the amplitude level. However, considering that the nucleon form factors are well known at small  $t$ , the BH process is precisely calculable.

## 2 Physics motivation: neutron GPDs and flavor separation

Measuring neutron GPDs is complementary to measuring proton GPDs: quark-flavor separation of the GPDs becomes possible only if both the proton and neutron GPDs are measured. Since we can express

$$\mathcal{H}^p(\xi, t) = \frac{4}{9}\mathcal{H}^u(\xi, t) + \frac{1}{9}\mathcal{H}^d(\xi, t) \quad (4)$$

and

$$\mathcal{H}^n(\xi, t) = \frac{1}{9}\mathcal{H}^u(\xi, t) + \frac{4}{9}\mathcal{H}^d(\xi, t) \quad (5)$$

(and similarly for  $\mathcal{E}$ ,  $\tilde{\mathcal{H}}$  and  $\tilde{\mathcal{E}}$ ), it immediately follows that

$$\mathcal{H}^u(\xi, t) = \frac{9}{15}(4\mathcal{H}^p(\xi, t) - \mathcal{H}^n(\xi, t)) \quad (6)$$

and

$$\mathcal{H}^d(\xi, t) = \frac{9}{15}(4\mathcal{H}^n(\xi, t) - \mathcal{H}^p(\xi, t)). \quad (7)$$

An extensive experimental program devoted to the measurement of GPDs using the DVCS channel on a proton target has been approved at Jefferson Lab, in particular with CLAS12. Single-spin asymmetries with polarized beam and/or linearly or transversely polarized proton targets, as well as unpolarized and polarized cross sections, will be measured with high precision and a vast kinematic coverage. If a similar program is performed on the neutron, the flavor separation of the various GPDs will be possible. An experiment to measure the beam-spin asymmetry for nDVCS, particularly sensitive to the GPD  $E_n$ , has already been approved [8]. The present proposal focuses on the extraction of two more observables, the target single-spin asymmetry and the (beam-target) double-spin asymmetry for nDVCS on a longitudinally polarized deuterium target. The next sections will outline those GPDs to which the nDVCS observables we plan to measure show the most sensitivity.

## 3 DVCS spin observables

A complete analysis of DVCS observables, including the asymmetries of interest in this document, in terms of Fourier harmonics with respect to the azimuthal angle, was carried out by Belitsky *et al.* [9], up to twist-3 approximation. These asymmetries allow the extraction of separate components of the azimuthal angular dependence of the  $eN \rightarrow eN'\gamma$  cross section, which are related to the Compton Form Factors (CFFs) defined in Eqs. 2-3. The cross section for exclusive photon production

$$\frac{d\sigma}{dx_B dy dt d\phi} = \frac{\alpha^3 x_B y}{16 \pi^2 Q^2 \sqrt{1 + \epsilon^2}} \left| \frac{\mathcal{T}}{e^3} \right|^2 \quad (8)$$

depends on the Bjorken variable  $x_B$ , the squared momentum transfer  $t = (P_1 - P_2)^2$  (where  $P_1$  and  $P_2$  are the four-momenta of, respectively, the initial and final nucleon), the lepton energy fraction  $y = P_1 \cdot q_1 / P_1 \cdot k$ , with  $q_1 = k - k'$  (where  $k$  and  $k'$  are the four momenta of, respectively, the incoming and scattered electron) and the angle  $\phi$ , which is the angle between the leptonic and hadronic planes, as shown in Fig. 2. We define  $\epsilon = 2x_B \frac{M}{Q}$ . The amplitude  $\mathcal{T}$

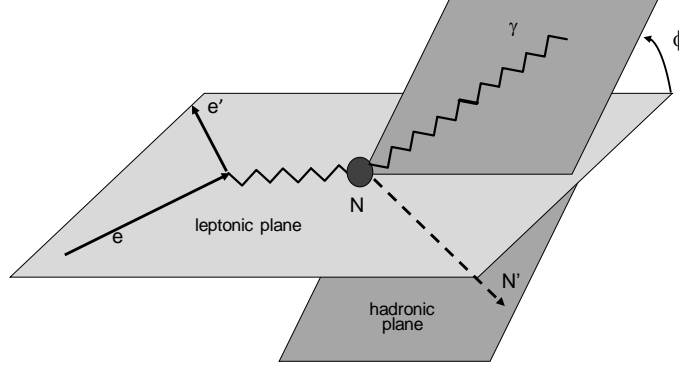


Figure 2: Schematic to illustrate the definition of the angle  $\phi$ , formed by the leptonic and hadronic planes, in the  $eN \rightarrow eN'\gamma$  reaction.

is the sum of the DVCS  $\mathcal{T}_{\text{DVCS}}$  and Bethe-Heitler (BH)  $\mathcal{T}_{\text{BH}}$  amplitudes.

The azimuthal angular dependence of each of the three terms in

$$\mathcal{T}^2 = |\mathcal{T}_{\text{BH}}|^2 + |\mathcal{T}_{\text{DVCS}}|^2 + \mathcal{I}, \quad (9)$$

where  $\mathcal{I}$  is the interference term

$$\mathcal{I} = \mathcal{T}_{\text{DVCS}} \mathcal{T}_{\text{BH}}^* + \mathcal{T}_{\text{DVCS}}^* \mathcal{T}_{\text{BH}}, \quad (10)$$

is given by [9]:

$$\begin{aligned} |\mathcal{T}_{\text{BH}}|^2 &= \frac{e^6}{x_B^2 y^2 (1 + \epsilon^2)^2 t \mathcal{P}_1(\phi) \mathcal{P}_2(\phi)} \{c_0^{\text{BH}} + \\ &+ \sum_{n=1}^2 c_n^{\text{BH}} \cos(n\phi) + s_1^{\text{BH}} \sin(\phi)\}, \end{aligned} \quad (11)$$

$$\begin{aligned} |\mathcal{T}_{\text{DVCS}}|^2 &= \frac{e^6}{y^2 Q^2} \{c_0^{\text{DVCS}} + \sum_{n=1}^2 [c_n^{\text{DVCS}} \cos(n\phi) + \\ &+ s_n^{\text{DVCS}} \sin(n\phi)]\}, \end{aligned} \quad (12)$$



$$\begin{aligned} \mathcal{I} = & \frac{e^6}{x_B y^3 t \mathcal{P}_1(\phi) \mathcal{P}_2(\phi)} \{ c_0^{\mathcal{I}} + \sum_{n=1}^3 [c_n^{\mathcal{I}} \cos(n\phi) + \\ & + s_n^{\mathcal{I}} \sin(n\phi)] \}, \end{aligned} \quad (13)$$

where  $\mathcal{P}_1$  and  $\mathcal{P}_2$  are lepton BH propagators (for more details and definitions, see [9]). The Fourier coefficients in  $|\mathcal{T}_{\text{BH}}|^2$  are calculable in QED, with knowledge of the nucleon form factors, while the ones appearing in  $\mathcal{I}$  and  $|\mathcal{T}_{\text{DVCS}}|^2$  depend on the Compton Form Factors.

### 3.1 Target-spin asymmetry

The use of a longitudinally polarized (LP) target allows the extraction of the target-spin asymmetry  $A_{\text{UL}}$  (here also referred to as TSA) which is given, at twist-2 level, by:

$$A_{\text{UL}}(\phi) \sim \frac{s_{1,\text{LP}}^{\mathcal{I}} \sin \phi}{c_{0,\text{unp}}^{\text{BH}} + (c_{1,\text{unp}}^{\text{BH}} + c_{1,\text{unp}}^{\mathcal{I}} + \dots) \cos \phi + \dots} \quad (14)$$

where the ellipses in the denominator represent smaller terms. The  $\sin \phi$  coefficient  $s_{1,\text{LP}}$ , originating from the DVCS/BH interference term, at leading-twist is proportional to a linear combination of the imaginary parts of the four CFFs,

$$\begin{aligned} s_{1,\text{LP}} & \propto \Im[F_1 \tilde{\mathcal{H}} + \xi(F_1 + F_2)(\mathcal{H} + \frac{x_B}{2} \mathcal{E}) + \\ & - \xi(\frac{x_B}{2} F_1 + \frac{t}{4M^2} F_2) \tilde{\mathcal{E}}], \end{aligned} \quad (15)$$

where  $F_1$  and  $F_2$  are, respectively, the Dirac and Pauli form factors. In the case of a proton target, the dominant contribution to  $A_{\text{UL}}$  comes from  $\Im \tilde{\mathcal{H}}_p$  and from  $\Im \mathcal{H}_p$ . **In the neutron case, for which  $F_2 \gg F_1$ , this observable is mostly sensitive to  $\Im \mathcal{H}_n$ .**

### 3.2 Double-spin asymmetry

The use of a polarized electron beam along with a polarized target allows also the determination of the double spin asymmetry  $A_{\text{LL}}$ . Unlike  $A_{\text{UL}}$ , the Bethe-Heitler process alone can generate a non-zero value for this observable. At twist-2 level, it takes the form:

$$A_{\text{LL}}(\phi) \sim \frac{c_{0,\text{LP}}^{\text{BH}} + c_{0,\text{LP}}^{\mathcal{I}} + (c_{1,\text{LP}}^{\text{BH}} + c_{1,\text{LP}}^{\mathcal{I}}) \cos \phi}{c_{0,\text{unp}}^{\text{BH}} + (c_{1,\text{unp}}^{\text{BH}} + c_{1,\text{unp}}^{\mathcal{I}} + \dots) \cos \phi \dots} \quad (16)$$

with

$$\begin{aligned} c_{0,\text{LP}}^{\mathcal{I}}, c_{1,\text{LP}}^{\mathcal{I}} & \propto \Re[F_1 \tilde{\mathcal{H}} + \xi(F_1 + F_2)(\mathcal{H} + \frac{x_B}{2} \mathcal{E}) + \\ & - \xi(\frac{x_B}{2} F_1 + \frac{t}{4M^2} F_2) \tilde{\mathcal{E}}], \end{aligned} \quad (17)$$

In this expression, the interference terms are expected to be smaller than the known BH terms. Moreover, both the constant and the  $\cos \phi$ -dependent terms contain contributions from both BH and the DVCS/BH interference. Nonetheless, it is expected that in some parts of the phase space  $A_{\text{LL}}$  has a measurable sensitivity to  $\Re \tilde{\mathcal{H}}_p$  (and, in a lesser way,  $\Re \mathcal{H}_p$ ), for the proton, **and to  $\Re \mathcal{H}_n$  for the neutron.**

## 4 Extraction of CFFs from fits to DVCS observables

In recent years, various groups have developed and applied different procedures to extract Compton Form Factors from DVCS observables. The approach adopted in this proposal [10, 11] has proved to be very effective and practical to extract GPD information from the existing proton DVCS data<sup>3</sup>. It is based on a local-fitting method at each given experimental  $(Q^2, x_B, -t)$  kinematic point. In this framework, instead of four complex CFFs defined as in Eqs. 2 and 3, there are eight real CFFs-related quantities (which, hereafter will be defined, for brevity, as “CFFs”)

$$F_{Re}(\xi, t) = \Re \mathcal{F}(\xi, t) \quad (18)$$

$$F_{Im}(\xi, t) = -\frac{1}{\pi} \Im \mathcal{F}(\xi, t) = [F(\xi, \xi, t) \mp F(-\xi, \xi, t)], \quad (19)$$

where the sign convention is the same as for Eq. 1. These CFFs are the almost-free<sup>4</sup> parameters, which are extracted from DVCS observables using the well-established DVCS+BH theoretical amplitude. The BH amplitude is calculated exactly while the DVCS one is taken at the QCD leading twist. The expression of these amplitudes can be found, for instance, in [12].

As there are eight CFF-related unknowns (four “real” CFFs, four “imaginary” ones) left as free parameters, including more observables, measured at the same kinematic points, will result in more tightly constrained fits and will increase the number and accuracy of CFFs extracted from them.

This was shown, for instance, with the analysis of the CLAS eg1-DVCS dataset [14], which was taken at 6 GeV with a longitudinally-polarized proton target. The simultaneous fit of three proton-DVCS asymmetries (BSA, TSA and DSA) lead to the extraction of  $\Im \mathcal{H}$  and  $\Im \tilde{\mathcal{H}}$ , as is shown in Fig. 3. These results for  $H_{Im}$  and  $\tilde{H}_{Im}$  confirmed what had been previously observed in a qualitative way by direct comparison of the  $t$ -dependence of the eg1-dvcs TSAs and the e1-dvcs BSAs in [15]: the  $t$ -slope of  $\Im \mathcal{H}$  is much steeper than that of  $\Im \tilde{\mathcal{H}}$ , hinting at the fact that the axial charge (linked to  $\Im \tilde{\mathcal{H}}$ ) might be more “concentrated” in the center of the nucleon than the electric charge (linked to  $\Im \mathcal{H}$ ). This is an interesting example of the nucleon tomography that becomes possible with the determination of CFFs, without the need for model input.

The main goal of the experiment proposed here is to provide, in a wide phase space, two kinds of asymmetries (single-target, and double beam-target), to be simultaneously fitted together with the beam-spin asymmetry that will be measured, at the same kinematic points, in the approved unpolarized-target experiment [8], and thus allow the extraction of the neutron CFFs. The results we expect to obtain are presented in Section 13.

## 5 Experimental situation

The determination of all the GPDs is clearly a non-trivial task, and requires measurement of several observables on both proton and neutron targets. Such a dedicated experimental program, concentrating on a proton target, has started worldwide in the past few years. Table 1

<sup>3</sup>Eventually, our results will also be compared to the various existing model parametrizations for the GPDs, the free parameters of which will be constrained by our data.

<sup>4</sup>The values of the CFFs are allowed to vary within  $\pm 5$  times the values predicted by the VGG model [12, 13].

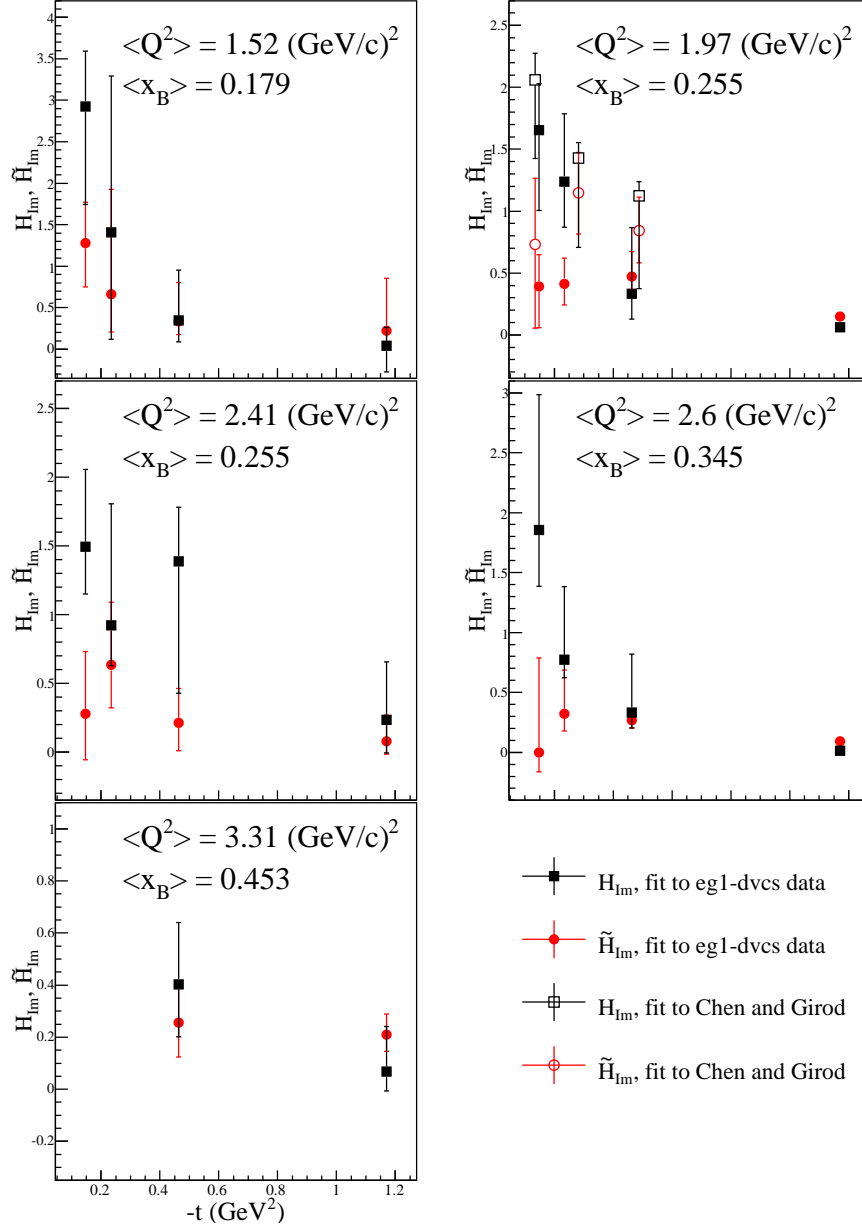


Figure 3:  $t$  dependence for each  $Q^2$ - $x_B$  bin of  $H_{Im}$  (black squares) and  $\tilde{H}_{Im}$  (red circles). The full points are obtained by fitting the eg1-DVCS data (TSA, BSA and DSA) [14]. The empty points were obtained by fitting the BSA results from [16] integrated over all values of  $Q^2$  at  $x_B \sim 0.25$ , and the TSAs from [17].

Observable (target)	Sensitivity to CFFs	Completed experiments	12-GeV experiments
$\Delta\sigma_{beam}(p)$	$\Im\mathcal{H}_p$	Hall A [19],[26] <sup>5</sup> , CLAS [22]	Hall A [23], CLAS12 [24] Hall C [27]
BSA(p)	$\Im\mathcal{H}_p$	HERMES [21], CLAS [20, 16, 14]	CLAS12 [24]
TSA(p)	$\Im\tilde{\mathcal{H}}_p, \Im\mathcal{H}_p$	HERMES [21], CLAS [17, 15, 14]	CLAS12 [24]
DSA(p)	$\Re\mathcal{H}_p, \Re\mathcal{H}_p$	HERMES [21], CLAS [14]	CLAS12 [24]
tTSA(p)	$\Im\mathcal{H}_p, \Im\mathcal{E}_p$	HERMES [21]	CLAS12 [25]
$\Delta\sigma_{beam}(n)$	$\Im\mathcal{E}_n$	Hall A [18],[28] <sup>5</sup>	
BSA(n)	$\Im\mathcal{E}_n$		CLAS12 [8]

Table 1: Summary of all existing data on proton and neutron DVCS spin observables, along with their sensitivity to the various GPDs. The “t” prefix indicates transversely polarized target.

summarizes the current situation. It is evident that while data exist for all proton observables, neutron DVCS data is woefully lacking. The only existing nDVCS experiment was performed in Hall A [18], where the beam-polarized cross section difference was extracted, albeit with small kinematical coverage, low statistical precision, and high systematic uncertainties. There also exists a number of approved 12 GeV pDVCS experiments at JLab, both in Hall A and Hall B, but only one approved neutron experiment, to measure the beam-spin asymmetries using CLAS12 [8]. While the new pDVCS experiments will greatly increase both the coverage and statistics of the existing proton data, we propose to further advance the nDVCS program by performing the first ever measurements of target-spin and double-spin asymmetries on a longitudinally polarized neutron target.

## 6 Experimental setup

A dynamically polarized  $^{14}\text{ND}_3$  target, described below, will provide the polarized neutrons on which the 11-GeV polarized electron beam from the upgraded CEBAF will be rastered. In order to map the complex kinematic dependence of the GPDs, a wide acceptance detector is necessary. For this experiment, we plan to use the CLAS12 detector (Fig. 4), which will be devoted to the detection of the electron, the neutron (in the Central Neutron Detector, described in Section 6.2) and the DVCS-BH photons. The CLAS12 acceptance for photons reaches down to polar angles of about  $5^\circ$  with the EC.

### 6.1 Polarized target

The proposed experiment will utilize a new, dynamically polarized target under construction for the CLAS12 spectrometer by a collaboration of the Jefferson Lab Target Group, the University of Virginia, Old Dominion University and Christopher Newport University. The target

---

<sup>5</sup>Analysis underway.

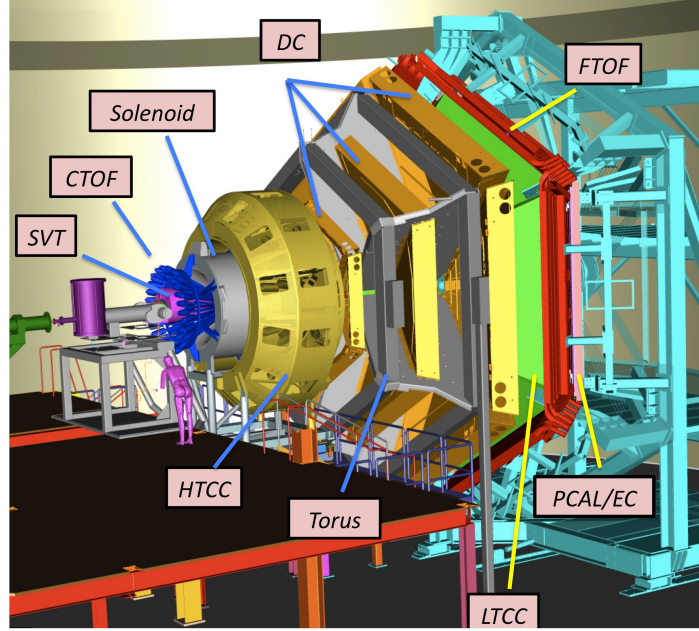


Figure 4: The CLAS12 detector and its components. In the forward part, the six coils of the superconducting toroidal magnet segment the detector into six sectors, each equipped with three regions of drift chambers (DC), High- and Low-Threshold Cherenkov Counters (HTCC and LTCC), Pre-Shower and Electromagnetic Calorimeters (PCAL and EC) and Forward Time-of-Flight (FTOF) scintillators. The central detector surrounds the target and is contained inside a solenoid magnet; its base equipment is composed of the Silicon Vertex Tracker (SVT) and the Central Time-of-Flight (CTOF).

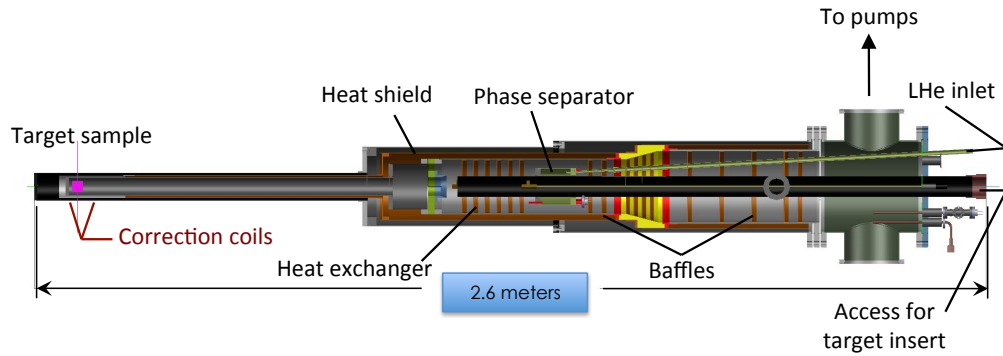


Figure 5: Side view of the CLAS12 dynamically polarized target.

cryostat, shown schematically in Figure 5, is specifically designed according to the geometrical constraints imposed by the CLAS12 detector package, primarily the Silicon Vertex Tracker. Frozen, deuterated ammonia has been chosen as the target material for its high deuteron content (30% by weight), high deuteron polarization (up to 50%), and high resistance to radiation damage [30]. Construction of the target is currently underway, with initial tests anticipated in 2017.

To realize Dynamic Nuclear Polarization (DNP), a dielectric solid is doped with a small concentration ( $10^{19} \text{ cm}^{-3}$ ) of paramagnetic radicals. The unpaired electrons in the radicals are highly polarized by cooling the sample to a low temperature and applying a strong magnetic field. For example, at the proposed operating conditions of 1 K and 5 T, the electron polarization is greater than 99.99%. Off-center microwave saturation of the electron spin resonance drives mutual electron/nuclear spin flips which effectively transfer the electron polarization to the nuclei. Either positive or negative nuclear polarization can be realized, depending on whether the microwave frequency is slightly below or above the electron resonance frequency of 140 GHz.

The target sample will be cooled to 1 K by a bespoke  $^4\text{He}$  evaporation refrigerator with an anticipated cooling power of about 0.5 W at 1.0 K. The CLAS12 solenoid shall provide the necessary 5 T magnetic field. For optimum polarization, the uniformity of the field should be about 100 ppm or better over the volume of the sample. If the solenoid is unable to provide this level of uniformity, it may be necessary to include small superconducting correction coils inside the target cryostat, or to reduce the sample dimensions.

### 6.1.1 Luminosity

The nominal length of the target container will be  $L = 4.0 \text{ cm}$ , with a 2.5 cm diameter. It will be filled with mm-sized granules of frozen  $^{14}\text{ND}_3$  with a density  $\rho = 1.007 \text{ g/cm}^3$  and a packing fraction  $f \approx 0.6$ . The total luminosity with electron beam intensity  $I$  will be

$$\begin{aligned} \mathcal{L} &= f\rho L N_A I \\ &= 0.6(1.007 \text{ g/cm}^3)(4.0 \text{ cm})(6.02 \times 10^{23} \text{ g}^{-1})(6.24 \times 10^9 \text{ s}^{-1} \text{ nA}^{-1}) \\ &= 9.1 \times 10^{33} \text{ cm}^{-2} \text{ s}^{-1} \text{ nA}^{-1} \end{aligned} \tag{20}$$

Note that this number is per nA of incident beam current. The luminosity for scattering from polarized neutrons within the deuterons will be 3/20 of the above number, or  $1.4 \times 10^{33} \text{ cm}^{-2} \text{ s}^{-1} \text{ nA}^{-1}$ . We anticipate running the experiment at 10 nA, giving a neutron luminosity of  $1.4 \times 10^{34} \text{ cm}^{-2} \text{ s}^{-1}$ . In order to reduce effects due to localized beam heating and radiation damage, the beam will be continuously rastered over 2.4 cm of the 2.5 cm target diameter.

### 6.1.2 Polarization measurement

The deuteron polarization will be monitored online by continuous wave NMR, using the industry standard Liverpool Q-meter [31]. There are two means whereby the polarization can be extracted from the NMR signal: the area method and the peak-height method. We intend to use both, and either should provide a relative uncertainty  $\Delta P/P \approx 4\%$ . We also intend to extract the polarization offline using the quasi-elastic scattering asymmetry.

First, the total area of the NMR absorption signal is proportional to the vector polarization of the sample, and the constant of proportionality can be calibrated against the polarization of the sample measured under thermal equilibrium (TE) conditions. This is the standard method used for polarized proton targets, but can be more problematic for deuteron targets. Typical conditions for the TE measurements are 5 T and 1.4 K, where the deuteron polarization is only 0.075%, compared to 0.36% for protons. This smaller polarization, along with quadrupolar broadening, makes the deuteron TE signal more difficult to measure with high accuracy. We therefore intend to implement a straightforward modification to the NMR circuit that has been shown to improve the stability and signal-to-noise ratio of the NMR signal [32]. This modification was successfully utilized during the eg1-DVCS experiment in Hall B.

Second, the deuteron polarization can also be extracted from the *shape* of the NMR signal. The deuteron is a spin-1 nucleus with three magnetic substates,  $m = -1, 0, +1$ , and the NMR absorption signal is a superposition of the  $-1 - 0$  and  $+1 - 0$  transitions. In the case of  $^{14}\text{ND}_3$ , the deuteron's electric quadrupole moment interacts with electric field gradients within the molecule and splits the degeneracy of the two transitions. The degree of splitting depends on the angle between the magnetic field and direction of the electric field gradient. The resultant line shape, integrated over a sample of many polycrystalline beads, has the form of a Pake doublet (see Fig.6). It has been experimentally demonstrated that, at or near steady-state conditions, the magnetic substates of deuterons in dynamically polarized  $^{14}\text{ND}_3$  are populated according to the Boltzmann distribution with a characteristic *spin* temperature  $T_s$  that can be either positive or negative, depending on the sign of the polarization. In this case, the vector polarization can be determined by the ratio of the two transition intensities,  $r = I_+/I_-$  [33]:

$$P_z = \frac{(r^2 - 1)}{(r^2 + r + 1)}. \quad (21)$$

An online estimate of the polarization can be made by comparing the heights of the two peaks. For a more accurate determination, an offline analysis of the entire line shape is necessary [33].

Finally, the polarization will also be studied offline using the experimental data. We will extract the product of the beam and target polarization,  $P_b P_t$ , by measuring the quasi-elastic asymmetry ( $\vec{d}(e, e'p)$ ) and by comparing it with the known theoretical value:

$$P_b P_t = \frac{1}{D_f} \frac{A_{meas}}{A_{theo}} \quad (22)$$

where  $D_f$  is the dilution factor to account for the contribution of the unpolarized background (Section 10). The target polarization value, needed for the TSA, will be then computed by taking the ratio of  $P_b P_t$  and the value of the beam polarization  $P_t$ , measured in dedicated Møller polarimetry runs.

### 6.1.3 Overhead for target operation

There are four routine target operations that must be considered as overhead. First, we intend to provide an initial dose of approximately  $20 \text{ Pe}^-/\text{cm}^2$  at 200 nA to each target sample prior to its use in the nDVCS experiment.<sup>6</sup> This is necessary to achieve the highest possible deuteron

---

<sup>6</sup>1  $\text{Pe}^- = 10^{15}$  electrons.

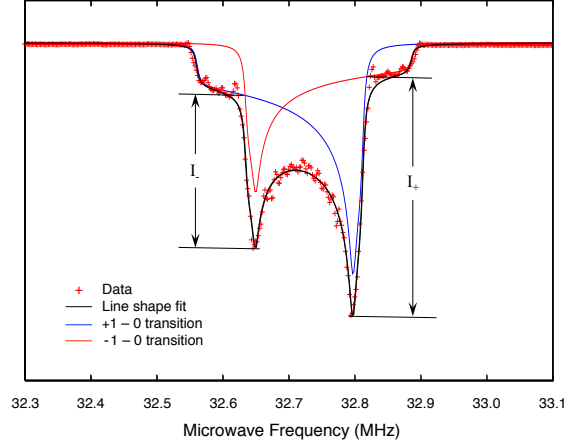


Figure 6: Typical NMR signal of polarized  $^{14}\text{ND}_3$ . The black line results from a sophisticated line shape analysis of the data points and is a superposition of the two NMR transitions shown in red and blue. This figure is adapted from [34].

polarization, as is explained below. Second, the target must be periodically warmed to approximately 100 K in order to repair the deleterious effects of radiation damage, a process known as annealing. Third, the target sample must be replaced when the anneals become ineffective at repairing the radiation damage. Fourth, the NMR system will be periodically calibrated by performing measurements of the thermal equilibrium polarization of deuterons at 5 T and temperatures around 1.4 K. We examine each of these in the following sections, and a summary is made at the end. Note that most overhead operations do not require the CEBAF electron beam, and are therefore counted as calendar days, not PAC days (one calendar day = two PAC days). The only exception is the initial cold dose of electrons, as described below.

**Cold dose** In solid ammonia, paramagnetic radicals are created within the target sample by ionizing radiation, usually in the form of a 10–20 MeV electron beam, at a dose of about  $100 \text{ Pe}^-/\text{cm}^2$ . This is usually applied with the material cooled to 90 K with liquid argon, after which it may be stored indefinitely in liquid nitrogen. In the case of *deuterated* ammonia, experience has shown that polarizations greater than 20% are only achieved after an additional “cold” dose of approximately  $10 \text{ Pe}^-/\text{cm}^2$  has been applied to the sample at 1 K. During the EG4 program in Hall B, the deuteron polarization increased from an initial value under 20% to more than 45% after a cold dose of  $20 \text{ Pe}^-/\text{cm}^2$  [35]. In this case, the CLAS detectors were turned off and a 100 nA beam was applied to the sample for an hour or so, followed by a 100 K anneal. These cold irradiations were interspersed with normal data-taking at 2 nA, and the deuteron polarization was observed to increase after each anneal, eventually exceeding 45%. Rather than following this prescription, we intend to prepare each target sample with a  $20 \text{ Pe}^-/\text{cm}^2$  cold dose before using it in the experiment. The CLAS12 detectors will be turned off for this procedure, which will require about a day for each sample at 200 nA.

**Annealing** As a solid polarized target material, deuterated ammonia has a remarkably high resistance to radiation damage, exceeded only by lithium hydride and lithium deuteride. When



exposed to ionizing radiation, the decay of the polarization is roughly exponential in manner,

$$P = P_0 e^{-D/\delta}. \quad (23)$$

Here  $D$  is the dose, measured in  $\text{Pe}^-/\text{cm}^2$ . The critical dose  $\delta$  of  $\text{ND}_3$  is different for the positive and negative spin states, with  $\delta_+ = 13 \text{ Pe}^-/\text{cm}^2$  and  $\delta_- = 26 \text{ Pe}^-/\text{cm}^2$  [30]. The polarization decay is due to the creation of additional paramagnetic species that do not contribute directly to the DNP process, but do contribute to the spin-lattice relaxation of the nuclear spins. Fortunately, the concentration of these new radicals can be reduced by annealing the target sample at temperatures up to about 100 K for some tens of minutes.

For the purposes of this proposal, we assume an initial polarization of 45%, which has been achieved in both the Hall C polarized target and the original Hall B polarized target. To maintain an average polarization of 40%, the radiation damage must be repaired by annealing the target sample when the polarization falls to 35%, or in other words, when the dose reaches  $-\ln(\frac{0.35}{0.45})\delta \approx 5 \text{ Pe}^-/\text{cm}^2$ . Here we have used the average value of  $\delta_+$  and  $\delta_-$ . Assuming a 10 nA beam current distributed evenly over a 2.4 cm diameter, this dose will be accumulated, on average, after 4 days. We estimate a total of four hours will be required to anneal the target, cool it back to 1 K, and repolarize it to 40–45%.

**Target lifetime** During 50 days of beam time at 10 nA, the polarized target will accumulate a total dose of  $60 \text{ Pe}^-/\text{cm}^2$ . However, the maximum that a  $\text{ND}_3$  sample can tolerate before it must be replaced is not fully known. McKee [36] reports that for the Gen01 experiment in Hall C, a total of dose of  $315 \text{ Pe}^-/\text{cm}^2$  was deposited on six different samples, and at least one continued to give high polarizations even after a dose of  $100 \text{ Pe}^-/\text{cm}^2$ . The total dose had little or no effect on the frequency of anneals, although the maximum attainable polarization did decline slightly after about  $50 \text{ Pe}^-/\text{cm}^2$ . For this proposal we make the conservative estimate that the samples will be replaced after a total dose of  $50 \text{ Pe}^-/\text{cm}^2$ , of which  $20 \text{ Pe}^-/\text{cm}^2$  will occur before data-taking begins. The remainder will be incurred after about 25 days of data-taking at 10 nA, and so we anticipate that two samples of  $\text{ND}_3$  will be sufficient for the entire experiment. Dedicated carbon runs will occur between the  $\text{ND}_3$  sample changes. The time required to replace an old  $\text{ND}_3$  sample with the carbon target, then replace the carbon with fresh  $\text{ND}_3$ , perform a TE calibration on the new sample and polarize it to 40–45% should be about 12 hours. Note that this does not include the actual time spent acquiring data on the carbon target.

**TE measurements** Thermal equilibrium (TE) measurements are necessary to calibrate the NMR system, and must be performed whenever a new target sample is introduced into the experiment. Additional measurements are made throughout the experiment in order to monitor and reduce sources of systematic uncertainty such as gain drift and settling of the sample beads. To perform a TE, the target sample must first have its existing dynamic polarization destroyed, either by temporarily warming the sample or temporarily lowering the magnetic field to zero. The sample must then be allowed to achieve its thermal equilibrium polarization, which it approaches in an exponential manner with a spin-lattice time constant  $T_1$  that depends on the field strength, the sample's temperature, and its density of paramagnetic radicals. Since annealing the sample reduces its radical density and increases  $T_1$ , it is best to do TEs prior to the anneals. Most measurements are made around 1.4 K, where the signal size is not too

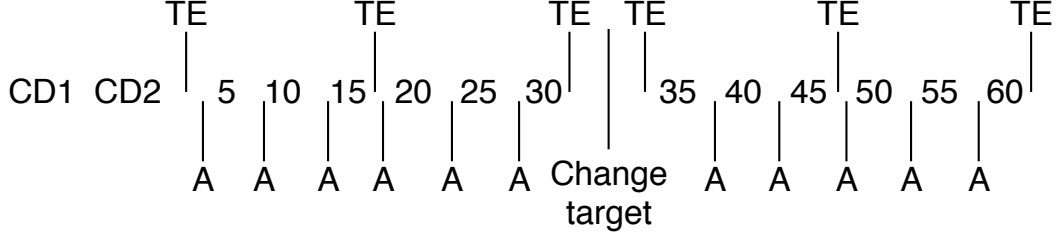


Figure 7: One possible sequence of target operations for the 50 day experiment. The numbers indicate the total dose accumulated during data taking, in  $\text{Pe}^-/\text{cm}^2$ . The experiment ends after  $60 \text{ Pe}^-/\text{cm}^2$ . **CD**: Cold Dose. **TE**: Thermal Equilibrium measurement. **A**: Anneal.

small, and  $T_1$  is not too long. Because the deuteron TE signal is small, a significant amount of signal averaging must be utilized to achieve a precise determination of its area, and so the time required for each measurement will depend strongly on the signal-to-noise ratio of NMR system. Based on past experience, we assume six hours will be sufficient. This includes the time required to polarize the sample to 40-45% at the end of the calibration.

**Target overhead summary** Based on the above information we provide the following estimate for the total overhead necessary to operate the polarized target. The total is 94 PAC hours, or about 4 PAC days. Whenever possible, anneals, TE measurements, and target changes can be coordinated with scheduled or unscheduled beam outages to lessen their impact on data acquisition and further reduce the overhead.

1. Cold dose of  $20 \text{ Pe}^-/\text{cm}^2$  at 200 nA. Required: 2 @ 24 hours each. Total: 48 PAC hours.
2. Anneal every  $5 \text{ Pe}^-/\text{cm}^2$ . Required: 11 @ 4 hours each. Total: 44 calendar hours = 22 PAC hours.
3. Change target sample after  $30 \text{ Pe}^-/\text{cm}^2$ . Required: 1 @ 12 hours each. Total: 12 calendar hours = 6 PAC hours.
4. TE calibration of NMR system at the beginning of each target sample, and after  $15 \text{ Pe}^-/\text{cm}^2$ . Required: 6 @ 6 hours each. Total: 36 calendar hours = 18 PAC hours.

## 6.2 Central Neutron Detector

The Central Neutron Detector was conceived to extend the CLAS12 acceptance for the recoil neutrons of nDVCS, which are expected to be mostly emitted between  $50^\circ$  and  $70^\circ$  [8]. The requirements of the detector are:

- good capabilities for neutron identification, via the measurement of  $\beta$  (with  $\beta = \frac{v}{c}$ ), for the kinematic range of interest ( $0.2 < p_n < 1.2 \text{ GeV}/c$ ,  $40^\circ < \theta_n < 80^\circ$ ) and

- neutron momentum resolution  $\sigma_P/P$  within 10%,

Early simulation studies [8] showed that these performances can be achieved by a scintillator-based detector providing a timing resolution of about 150 ps.

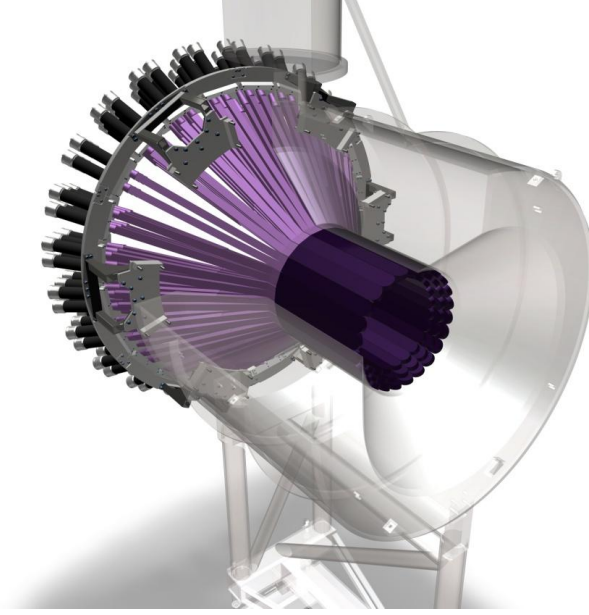


Figure 8: Design of the Central Neutron Detector, inserted in the CLAS12 solenoid.

The core of the CND (Fig. 8), which will be placed in the Central Detector, in the 10 cm of radial space left between the CTOF and the solenoid magnet, is a barrel, coaxial with the beam direction, made of three radial layers of trapezoidal plastic-scintillator bars. Each radial layer contains 48 bars, connected in pairs by a "u-turn" light guide at the downstream end. Photomultipliers are coupled to the upstream end of each scintillator via 1.5m-long light guides. For each hit, half of the light emitted in a scintillator paddle is collected by the upstream PMT (the "direct" signal), while the other half propagates through the u-turn and the neighboring paddle to the PMT connected at its end (the "indirect" signal).

Three such scintillator pairs (inner, middle, and outer) are grouped together to form a single, radial "block". The CND comprises 24 of these blocks, covering the entire azimuthal range (Fig. 9).

The assembly of the CND, which was entirely carried out at the IPN Orsay, started in December 2013, and was completed in February 2015. The detector was shipped and stored at JLab in June 2015, awaiting its installation in CLAS12. Upon assembly, each block of the CND was tested with cosmic rays, triggering on the triple-coincidence of the signal in all three layers. Data were taken for about one week for each block, and the block performances were studied, with special attention to the timing resolution. Figure 10 shows the raw distribution of TDCs as a function of ADCs for the six PMTs in one of the 24 blocks. Notice the clear separation between direct (low-TDC/high-ADC) and indirect (high-TDC/low-ADC) signals.

To define an average time resolution for our setup in the triple-coincidence trigger configuration, we use the method inspired by the work done in [37] and later adopted for the CLAS

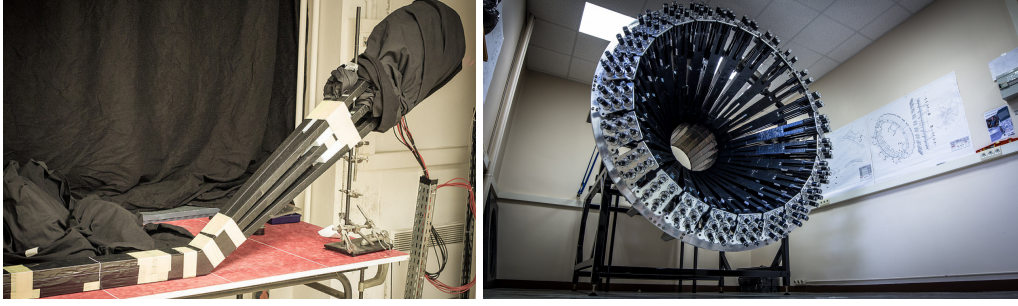


Figure 9: Construction and testing of the CND at Orsay. Left: one 2x3 block undergoing cosmic ray tests. Right: all 24 blocks installed into a mock-up of the CLAS12 solenoid.

TOF system [38].

The timing resolutions for all the CND blocks, computed according to the method of [38], are represented by the black triangles in Fig. 11. The average is 148.0 ps. As a cross check, the resolution was also computed using the method adopted by V. Baturin for the CLAS12 CTOF [39] (red triangles in Fig. 11, with average 149.3 ps). The results of the two methods are consistent. The resolutions of the 24 blocks are very close to the required 150 ps. The systematic uncertainty of our results is estimated to be about 7%, determined by repeating the measurements multiple times, and by comparing multiple subsets of each measurement.

Thus, for resolutions of 150 ps, we have a systematic uncertainty of about 10 ps.

It is also worth mentioning that the TDCs that will be used for the actual experiment will have a better resolution (25 ps/channel) than the ones used for these tests (50 ps/channel).

### 6.3 Simulation and reconstruction

In order to study the performances of this detector, and thus evaluate the projected results of the nDVCS experiment, its geometry (Fig. 12) has been added to the CLAS12 GEANT4-based simulation package, GEMC [40]. The energy loss of the particle in the scintillator material is converted to numbers of optical photons in accordance with Birk's formula [41], the resulting signal is propagated through the scintillator paddle, light guide and PMT, and the final charge and time are digitized to mimic the output from the ADC/TDC [42].

The timing resolution and the energy loss due to the u-turn geometry have been included in the simulation using the values measured in the cosmic-rays tests described in the previous section.

Simulations, which included all the other components of the Central Detector, have been run to evaluate the efficiency of the CND for neutrons, its ability to discriminate between neutrons and photons, and its angular and momentum resolutions. Neutrons and photons of momenta varying between 0.1 and 1 GeV/c and having polar angles  $\theta$  varying between  $50^\circ$  and  $70^\circ$  have been generated at fixed azimuthal angle ( $\phi = 0^\circ$ ), pointing to the center of one of the scintillator bars. The results obtained with these simulations are described here below.

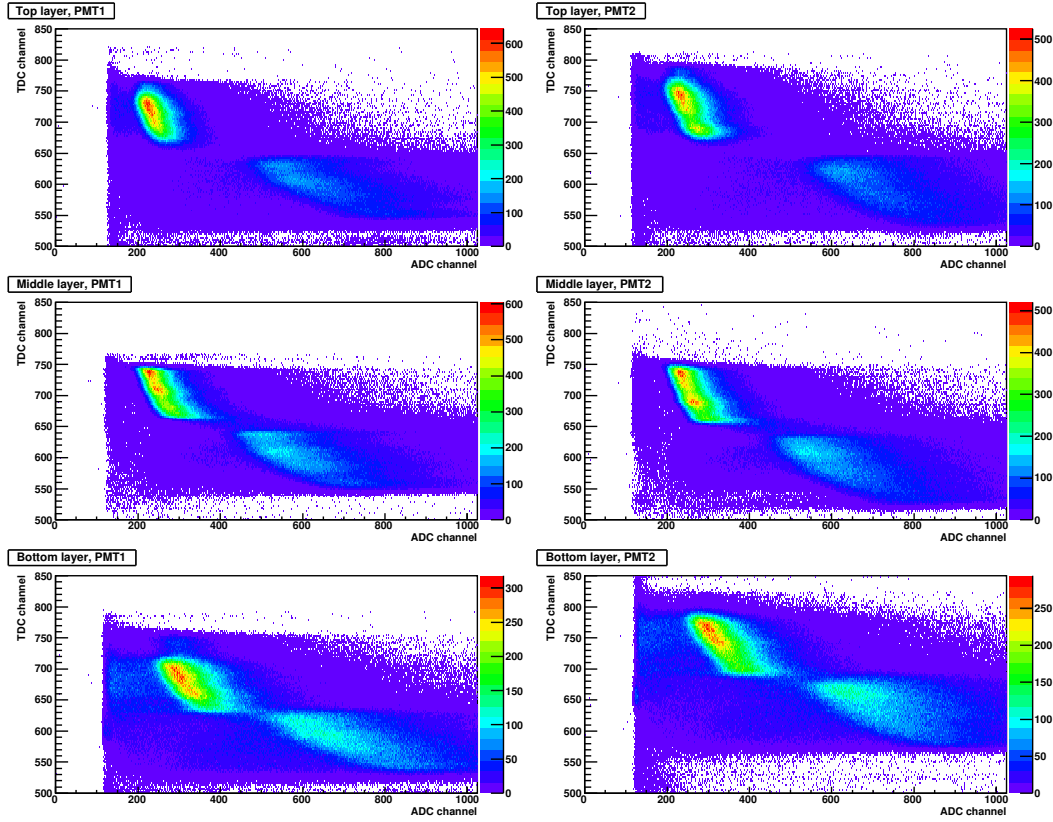


Figure 10: Cosmic rays data. Raw TDC vs ADC for each of the six PMTs of block 2 of the CND. No pedestal subtraction or data-cleaning cuts are applied.

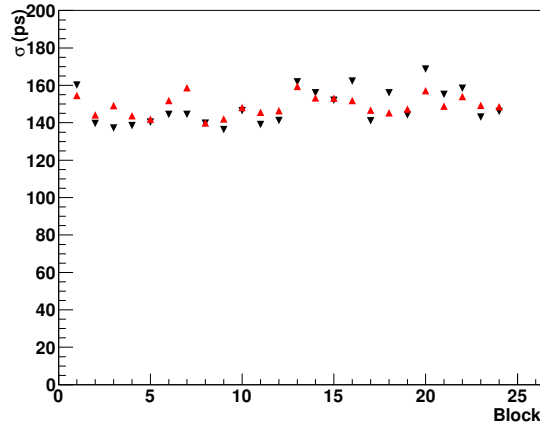


Figure 11: Average time resolution for each block of the CND from cosmic rays measurements in triple-coincidence. The black and red triangles are the results obtained with the formulae from, respectively, Refs. [38] and [39].

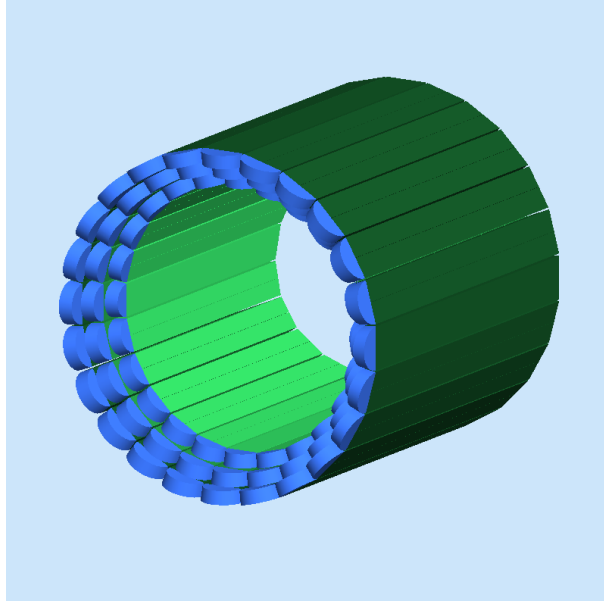


Figure 12: Geometry of the Central Neutron Detector in the GEMC simulation, showing three layers of scintillator paddles (green) coupled in pairs via u-turn light guides (blue) downstream.

### 6.3.1 Efficiency

The detection efficiency is defined here as the ratio between the number of events for which a good hit (i.e., a hit having deposited energy above a given threshold) was successfully reconstructed as a neutron in the correct azimuthal bin of the CND and the total number of neutrons generated. Several values of energy thresholds, between 1 and 5 MeV, have been tested. The efficiency decreases with increasing threshold, and ranges between 12% at the lowest thresholds and 7% at the highest ones. Figure 13 shows the efficiency as a function of the momentum of the neutrons, at a fixed energy threshold of 2 MeV, and for different values of  $\theta_n$ .

### 6.3.2 Angular and momentum resolutions

The resolutions on the polar angle  $\theta$  of the neutron that can be obtained with the CND are strongly linked to its TOF resolution. The angle  $\theta$  is in fact given by

$$\theta = (180/\pi) \cdot \arccos\left(\frac{z_{ave}}{l}\right) \quad (24)$$

where the reconstructions of the radial distance of the hit from the target,  $l$ , and of its position along the scintillator bar,  $z_{ave}$ , both depend on the time measurement. Using a value deduced from the measurements on the CND prototype to apply a gaussian smearing on the timing [8], the  $\theta$  resolution resulting from GEMC was studied as a function of neutron momentum and  $\theta$  itself. The results are shown in Fig. 14, where the angular resolution  $\sigma_\theta$ , obtained via gaussian fits of the simulated  $\theta$  distributions, is plotted as a function of  $\theta$ , for a particular value

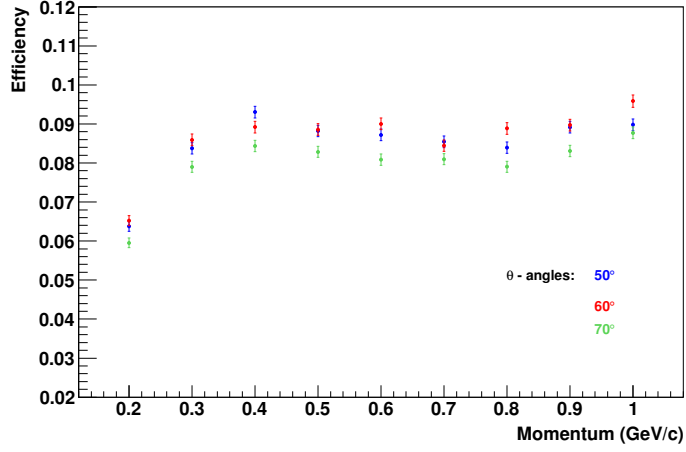


Figure 13: Efficiency for the detection of neutrons, as a function of neutron momentum, for a 2-MeV threshold on the deposited energy. The efficiency is shown for three different values of  $\theta_n$ , between  $50^\circ$  and  $70^\circ$ .

of neutron momentum (0.4 GeV/c).  $\sigma_\theta$  is seen to increase slightly with the angle, from  $1.5^\circ$  to  $3.5^\circ$ . It has also been found to be relatively insensitive to the neutron momentum.

The resolution on the azimuthal angle is directly connected to the total number of scintillator bars along  $\phi$ . In fact, the bin size  $\Delta\phi$  is given by

$$\Delta\phi = \frac{360^\circ}{N} = 7.5^\circ \quad (25)$$

where  $N$  is the total number of paddles in  $\phi$  (48 for the final design of the CND).  $\sigma_\phi$  can be taken as half of  $\Delta\phi$ , therefore  $3.75^\circ$ .

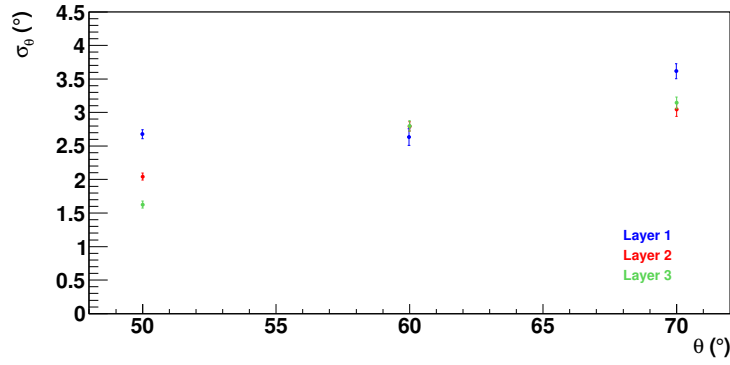


Figure 14: Angular resolution  $\sigma_\theta$  as a function of  $\theta$  for neutrons of momentum 0.4 GeV/c, for a 2-MeV threshold on the deposited energy. The three colors of the points correspond to the three radial layers of the CND.

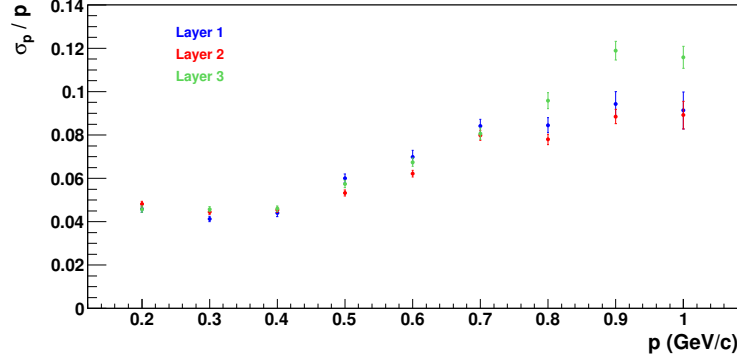


Figure 15: Momentum resolution  $\sigma_p/p$  as a function of  $p$  for neutrons having  $\theta = 60^\circ$ , for a 2-MeV threshold on the deposited energy. The three colors of the points correspond to the three radial layers of the CND.

The resolution on the neutron momentum, calculated after particle identification on the basis of  $\beta$ , according to the formula

$$p = \frac{\beta \cdot m_n}{\sqrt{1 - \beta^2}}, \quad (26)$$

is also strictly connected to the TOF resolution. Figure 15 shows the momentum resolution  $\sigma_p/p$  as a function of momentum for neutrons emitted with  $\theta = 60^\circ$ : it increases with increasing momentum, and ranges between 4% and 11%. No appreciable variations of momentum resolution are observed by varying the neutron polar angle.

### 6.3.3 Particle Identification

Since the charged particles passing through the CND will be vetoed by the Central Tracker, the only particles that could be mistaken for neutrons in the CND are the photons. The efficiency of the CND for detecting photons (Fig. 16) has been estimated in simulations to be similar to that for neutrons, about 10% for photon energies down to 0.2 GeV. The efficiency drops to zero for lower energy photons, depending on the threshold cut applied.

Neutrons can be discriminated from photons by means of their  $\beta$ , and so GEMC simulations have been performed to estimate the  $\beta$  distributions that may be obtained from the CND. Results for one of the three radial layers, integrated over the azimuthal angle, is shown in Figure 17. Here  $\beta$  distributions for neutrons with momenta between 0.2 and 1 GeV/c are compared with 1 GeV photons. Very clear separation is evident for neutrons less than about 0.9 GeV/c, which comprise over 90% of the expected nDVCS events.

This is evident also from Fig. 18, where the error bars correspond to  $3\sigma$ , where  $\sigma$  is the gaussian width of each  $\beta$  distribution. Equal neutrons and photon yields have been assumed for this study. This assumption has been justified with detailed studies on the different types of photonic backgrounds that can affect the CND [8].



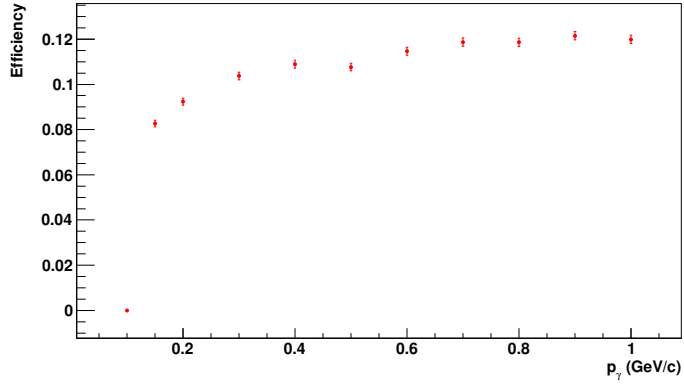


Figure 16: Efficiency for the detection of photons, as a function of photon momentum, for a 2-MeV threshold on the deposited energy. The efficiency is shown for  $\theta_\gamma = 60^\circ$ . Below  $E_\gamma = 0.15$  GeV, the photon efficiency drops to zero.

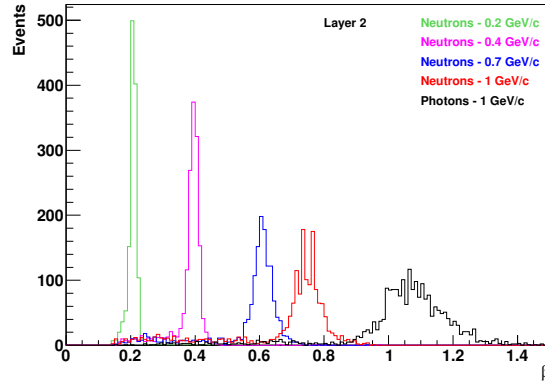


Figure 17:  $\beta$  distributions for neutrons with  $p_n = 0.2$  GeV/c (green),  $p_n = 0.4$  GeV/c (purple),  $p_n = 0.7$  GeV/c (blue),  $p_n = 1$  GeV/c (red), and photons with  $E = 1$  GeV, for the middle layer of the CND. The threshold on the deposited energy is 2 MeV. The plots show all hits, integrated over  $\phi$ . Equal neutron and photon yields have been assumed here.

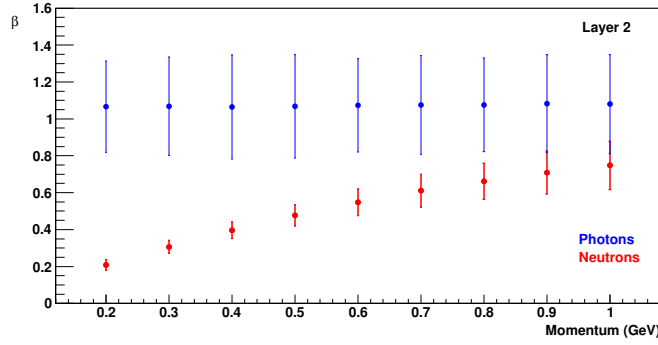


Figure 18:  $\beta$  versus momentum for neutrons (red) and photons (blue) with momenta between 0.2 and 1 GeV, for the middle layer of the CND. The error bars are defined as  $3\sigma$ , where  $\sigma$  is the fitted width of each  $\beta$  peak. The threshold on the deposited energy is 2 MeV.

## 7 nDVCS at CLAS12: kinematics and acceptances

In order to study the kinematics of the reaction and determine the expected count rates for both the nDVCS signal and its main background ( $ed \rightarrow en\pi^0(p)$ ), an event generator for DVCS/BH and exclusive  $\pi^0$  electroproduction on the neutron inside a deuterium target has been developed [44]. The DVCS amplitude is calculated according to the BKM formalism [9], where the GPDs have been taken from the standard CLAS DVCS generator [45]. The Fermi-motion distribution is calculated with the Paris potential [46]. The exclusive  $\pi^0$  electroproduction channel is generated assuming longitudinal dominance within the naive quark model approximation [44]. Note that no smearing effects due to the nuclear  $\text{ND}_3$  target are included in the event generator.

The output of the event generator was fed through CLAS12 FASTMC, to simulate the acceptance and resolutions of electrons and photons in the Forward Detector.

The expected resolutions and acceptance of the CND for neutrons, outlined in the previous sections, were also included in the FastMC code.

Kinematic cuts to ensure the applicability of the GPD formalism ( $Q^2 > 1 \text{ GeV}^2/c^2$ ,  $t > -1.2 \text{ GeV}^2/c^2$ ,  $W > 2 \text{ GeV}/c^2$ ) have been applied. Figure 19 shows the coverage in  $Q^2$ ,  $x_B$  and  $t$  that is obtained from the event generator for the nDVCS/BH reaction, with an electron-beam energy of 11 GeV.

Figures 20, 21, and 22 show the momentum  $p$  as a function of  $\theta$  in the lab frame for, respectively, the electron, the photon and the neutron. As expected, the electron and the photon are mostly emitted at forward angles, while the neutron recoils at backwards angles.

## 8 Measurement of the asymmetries

We plan to extract two kinds of asymmetries, the experimental definitions of which are given here. In all of the formulae below, the first sign in the superscript on the number of normalized DVCS/BH events  $N$  is the beam helicity ( $b$ ) and the second sign is the target polarization ( $t$ ).

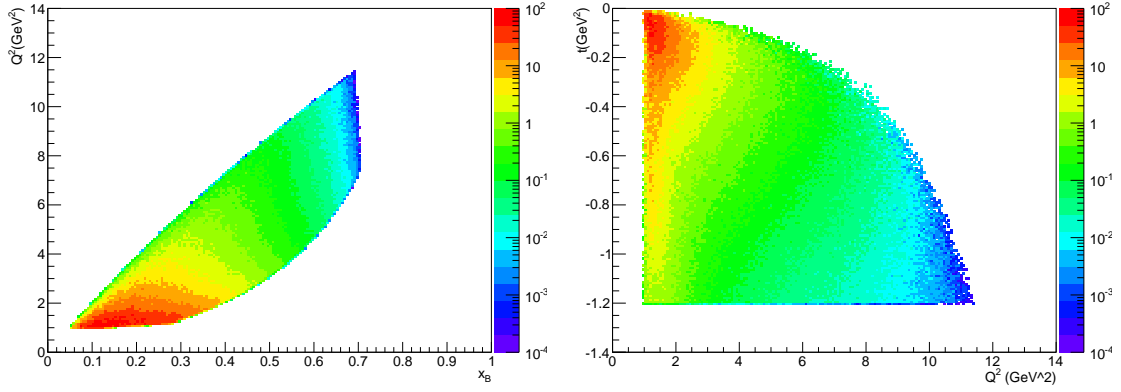


Figure 19: Distributions of kinematic variables for nDVCS events. CLAS12 acceptance cuts and physics cuts are included. Left:  $Q^2$  as a function of  $x_B$ . Right:  $t$  as a function of  $Q^2$ .

$N$  is obtained from  $en\gamma$  events ( $N_{en\gamma}$ ), normalized by the corresponding Faraday-cup charge ( $FC^{bt}$ ) after subtraction of the  $\pi^0$  background as follows:

$$N^{bt} = (1 - B_{\pi^0}^{bt}) \cdot \frac{N_{en\gamma}^{bt}}{FC^{bt}}, \quad (27)$$

where  $B_{\pi^0}$  is the relative  $\pi^0$  contamination, outlined in Section 9.

The target-spin asymmetry will be computed as:

$$A_{UL} = \frac{N^{++} + N^{-+} - N^{+-} - N^{--}}{D_f(P_t^-(N^{++} + N^{-+}) + P_t^+(N^{+-} + N^{--}))}. \quad (28)$$

$D_f$  is the dilution factor to account for the contribution of the unpolarized background (Section 10), and  $P_t$  is the polarization of the target.

The double (beam-target) spin asymmetry will be obtained as:

$$A_{LL} = \frac{N^{++} + N^{--} - N^{+-} - N^{-+}}{P_b \cdot D_f(P_t^-(N^{++} + N^{-+}) + P_t^+(N^{+-} + N^{--}))} \quad (29)$$

where  $P_b$  is the polarization of the beam.

In the following, the steps leading to the extraction from the data of all the terms composing these asymmetries will be presented.

## 8.1 Event selection and exclusivity cuts

After selecting events with exactly one electron (in the forward part of CLAS12) and one neutron (in the CND and in the EC), and at least one photon (in the EC), and applying the appropriate PID and fiducial cuts, further cuts need to be applied to ensure the exclusivity of the DVCS/Bethe-Heitler final state. Two kinds of backgrounds need, in fact, to be removed, or reduced as much as possible: the nuclear background coming from scattering on the nitrogen of

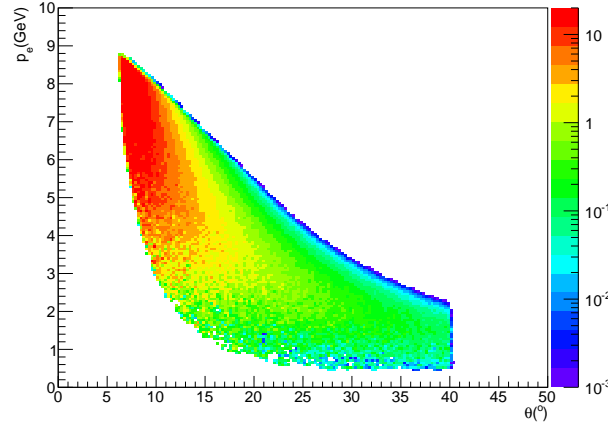


Figure 20: Electron momentum as a function of electron polar angle, for nDVCS events. CLAS12 acceptance cuts and physics cuts are included.

the  $\text{ND}_3$  target, and the background coming from other channels containing electron, neutron and at least one photon in the final state. Having measured the four-vectors of the three active final-state particles, one can construct several observables (hereafter referred to as “exclusivity variables”) on which cuts can be applied to select the DVCS/BH channel. Here, the following quantities were studied, with the aid of our nDVCS and  $en\pi^0(p)$  simulations:

- the squared missing mass of  $X$ , in the  $ed \rightarrow en\gamma X$  reaction;
- the momentum of the spectator proton, obtained as  $p(X)$  from  $ed \rightarrow en\gamma X$ ;
- the squared missing mass of  $X$ , in the  $en \rightarrow en\gamma X$  reaction, assuming the initial neutron to be at rest;
- the missing energy of  $X$ , in the  $ed \rightarrow en\gamma X$  reaction;
- $p_{\text{perp}}$ , the transverse component of the missing momentum of the reaction  $en \rightarrow en\gamma X$ , given by  $p_{\text{perp}} = \sqrt{p_x(X)^2 + p_y(X)^2}$ .

Figures 23 and 24 show the exclusivity variables listed above for, respectively, nDVCS simulated events and  $en\pi^0(p)$  simulated events for which only one electron, one neutron and one photon of energy above 2 GeV fell within the CLAS12 acceptance. The red lines represent the exclusivity cuts, the values of which were chosen to maximize the number of nDVCS events retained while reducing the  $en\pi^0(p)$  background as much as possible. It must be stressed that the event generator adopted here does not contain Fermi motion effects coming from the nitrogen of the  $\text{ND}_3$  target. The experimental distributions of the exclusivity variables will therefore be broader, and the peaks will be masked by the nuclear background. However, it was shown in the eg1-DVCS analysis [14] that peaks due to the pDVCS channel became evident when appropriately rescaled spectra from a  $^{12}\text{C}$  background target were subtracted from the exclusivity variable distributions. We plan to adopt a similar approach here.

The expected  $en\pi^0(p)$  contamination that remains after these cuts is shown in Fig. 25, where the ratio of surviving  $en\pi^0(p)$  events to the number of nDVCS events is plotted as a function of  $\phi$ , integrated over the other kinematic variables. It ranges from 0, at the extreme  $\phi$

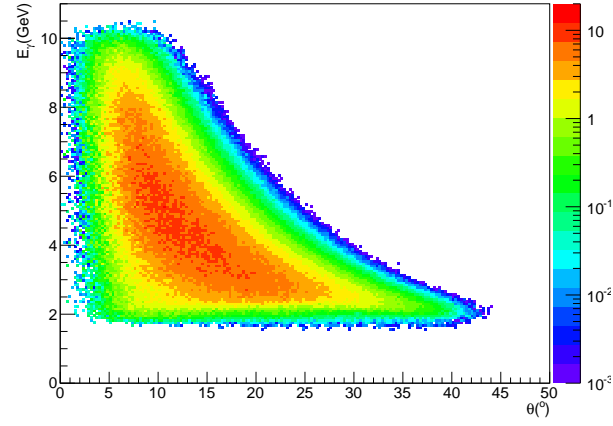


Figure 21: Photon momentum as a function of photon polar angle, for nDVCS events. CLAS12 acceptance cuts and physics cuts are included.

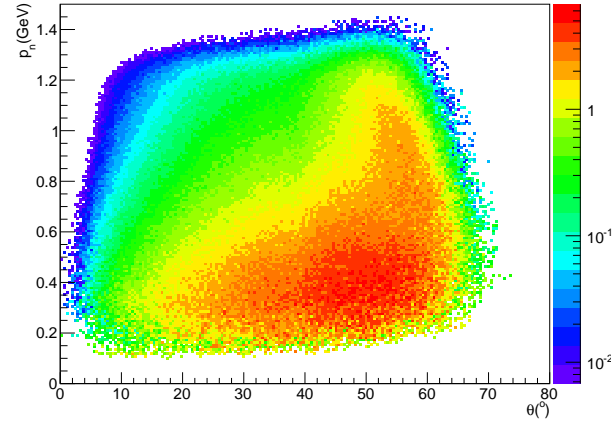


Figure 22: Neutron momentum as a function of neutron polar angle, for nDVCS events. CLAS12 acceptance cuts and physics cuts are included.

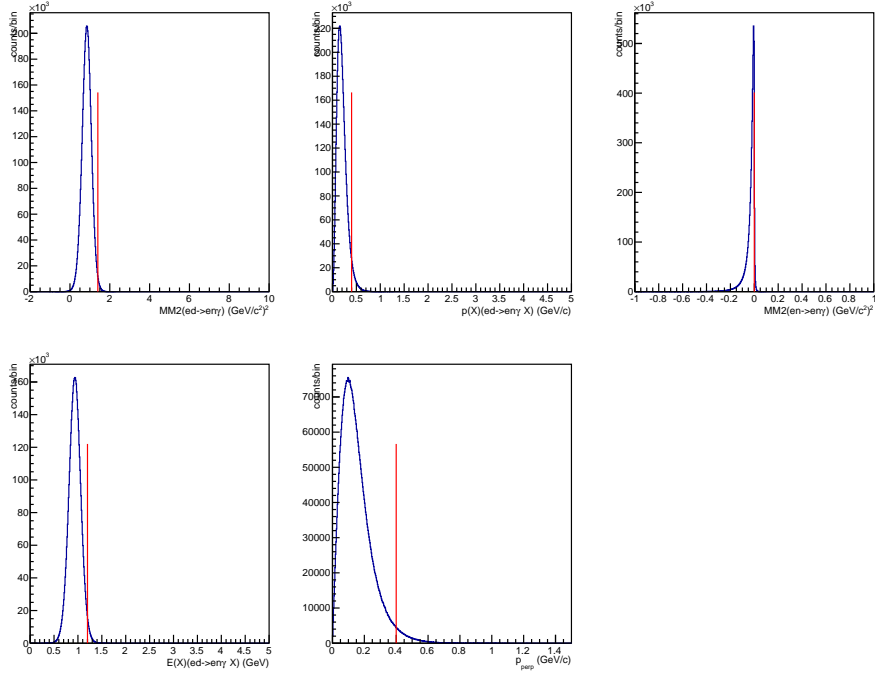


Figure 23: nDVCS simulation, after FastMC: DVCS exclusivity variables. Starting from the top left:  $MM_X^2(ed \rightarrow en\gamma X)$ ,  $p(X)(ed \rightarrow en\gamma X)$ ,  $MM_X^2(en \rightarrow en\gamma X)$ ,  $E(X)(ed \rightarrow en\gamma X)$ ,  $p_{perp}$ . The red lines mark the values adopted for the nDVCS exclusivity cuts.

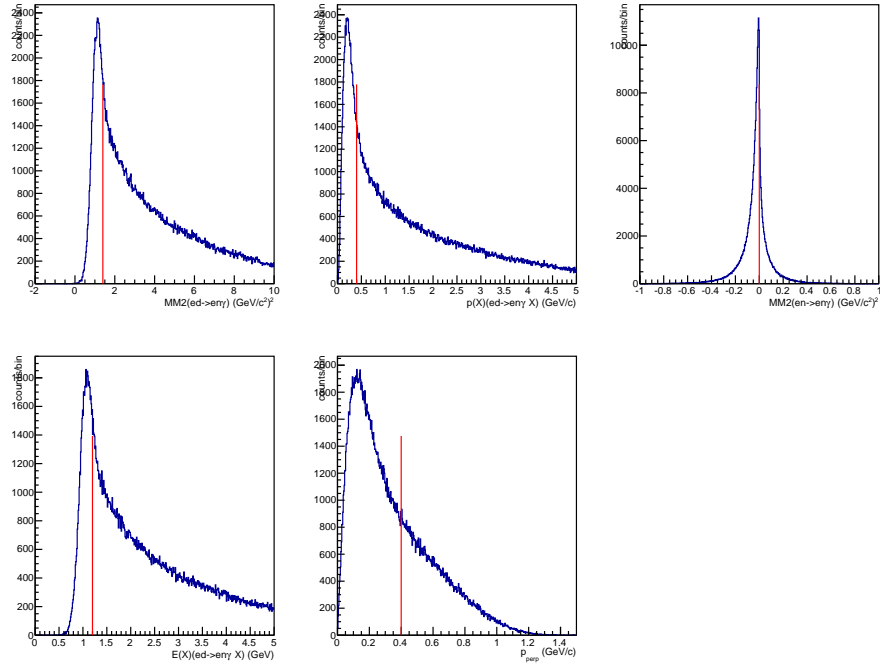


Figure 24:  $\pi^0$  simulation, after FastMC, events for which only one electron, one neutron and one photon of energy above 2 GeV fell within the CLAS12 acceptance: DVCS exclusivity variables, same as Fig. 23. The red lines mark the values adopted for the nDVCS exclusivity cuts.

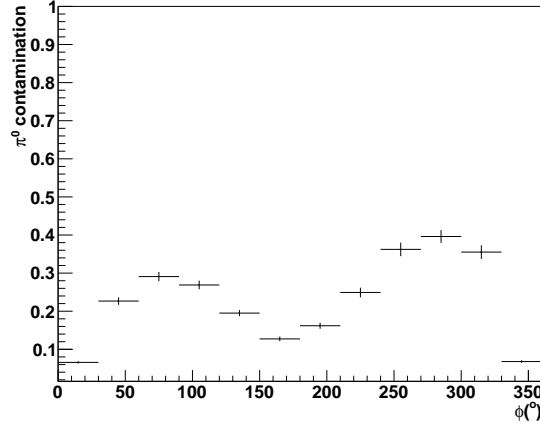


Figure 25: Expected  $\pi^0$  contamination fraction for the proposed experiment, defined as  $\frac{N_{\pi^0 1\gamma}}{N_{en\gamma}}$ , as a function of  $\phi$  and integrated over the other kinematic variables.

values, to about 40%, in the central  $\phi$  range. This background can be evaluated and subtracted from the final asymmetries, as will be described in Section 9.

An exploratory nDVCS analysis on the ND<sub>3</sub> subset (“part C”) of the CLAS eg1-dvcs dataset is underway [47]. In spite of the very poor statistics and the far from optimal neutron reconstruction in the CLAS EC calorimeters, a selection of the nDVCS final state has been possible. Figure 26 shows the same exclusivity variables as are plotted in Fig. 23, obtained after applying nDVCS selection cuts to the  $en\gamma$  event sample, which were optimised for the eg1-dvcs data. The similarities with our simulations are remarkable, especially considering that no nuclear background was subtracted from the distributions of Fig. 26, which gives confidence in this data-selection technique for the proposed experiment. Additionally, the effect of nuclear background subtraction can be seen in Fig. 27, which shows the missing mass squared from  $en \rightarrow enX$  before and after subtraction of opportunely scaled distributions obtained with carbon data, and in Fig. 28, displaying the carbon-subtracted  $m_X^2$  distribution from  $en \rightarrow en\gamma X$ . The figure indicates that a good selection of the  $en\gamma$  final state has been possible even within the limitations of the eg1-dvcs experiment and illustrate the applicability of the technique to the proposed experiment.

## 9 Neutral pion background

Once the events containing one electron, one neutron and one photon are selected, the nDVCS/BH final state can be isolated by cutting on the  $en\gamma$  missing mass and other exclusivity variables. However, due to the finite resolutions of the detectors, the final event sample will still be contaminated by  $en\gamma$  events coming from the  $en\pi^0(p)$  channel, where one photon from the  $\pi^0$  decay is detected in the forward part of CLAS12 while the other escapes detection. This contamination will be evaluated and subtracted as was done in previous DVCS CLAS analyses [16, 15, 14, 22], by extracting exclusive  $en\pi^0(p)$  events — detecting both decay photons — from the data, and using Monte Carlo simulations to evaluate the ratio of acceptances of



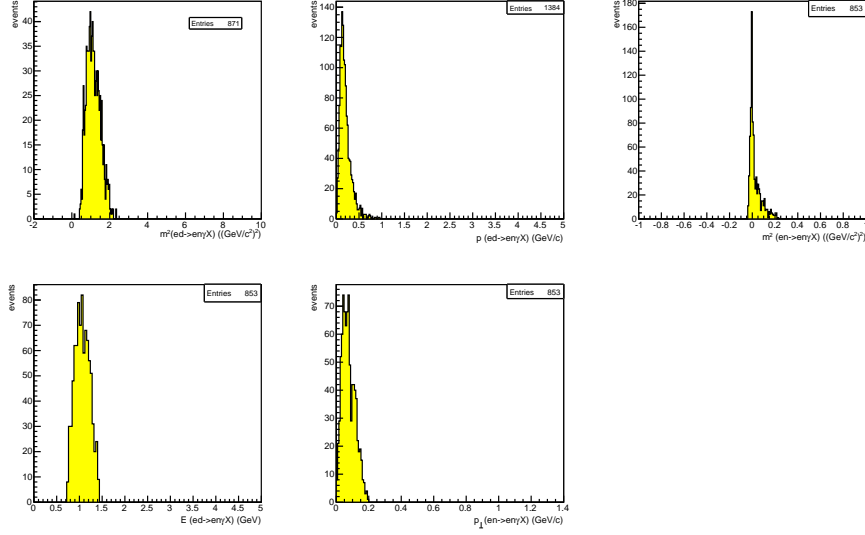


Figure 26: nDVCS analysis of the CLAS eg1-dvcs data set, after exclusivity cuts: DVCS exclusivity variables, same as Fig.23.

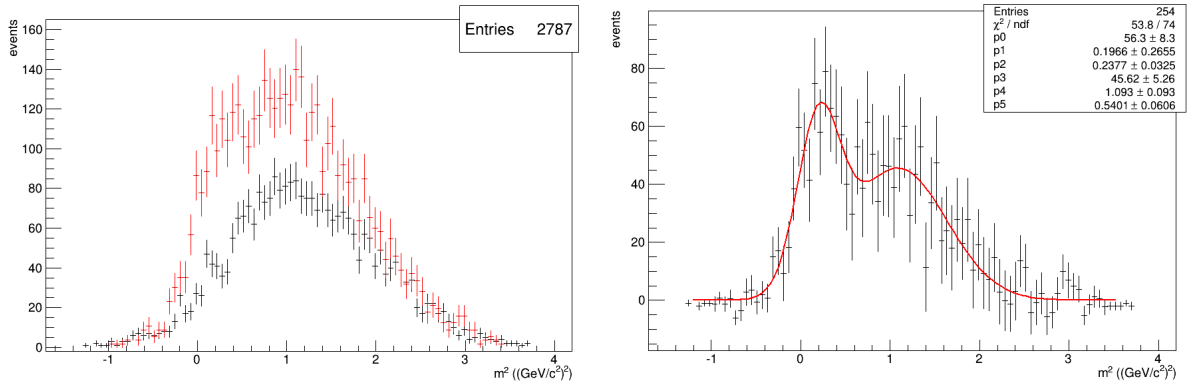


Figure 27: nDVCS analysis of the CLAS eg1-dvcs data set. Left: squared missing mass of  $X$  in  $en \rightarrow enX$ , with  $\text{ND}_3$  (red) and carbon (black); right: after carbon subtraction, a peak near 0 appears.

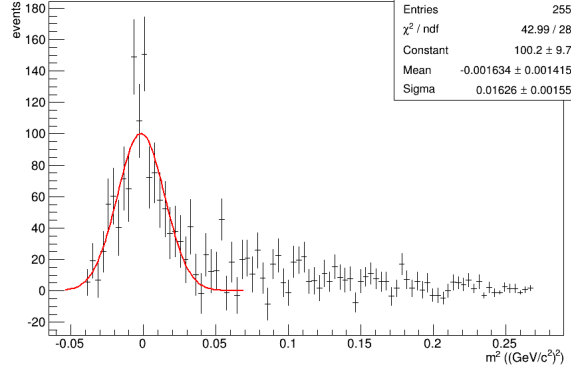


Figure 28: nDVCS analysis of the CLAS eg1-dvcs data set: squared missing mass of  $X$  in  $en \rightarrow en\gamma X$ , after exclusivity cuts and carbon subtraction.

$\pi^0$  events with 1 and 2 photons detected. The final number of nDVCS/BH events, in each 4-dimensional bin, will be obtained as:

$$N_{DVCS}(Q^2, x_B, -t, \phi) = N_{en\gamma}(Q^2, x_B, -t, \phi) - N_{\pi^0 1\gamma}(Q^2, x_B, -t, \phi) \quad (30)$$

where

$$N_{\pi^0 1\gamma}(Q^2, x_B, -t, \phi) = N_{\pi^0}^{data}(Q^2, x_B, -t, \phi) \cdot \frac{N_{\pi^0 1\gamma}^{MC}(Q^2, x_B, -t, \phi)}{N_{\pi^0 2\gamma}^{MC}(Q^2, x_B, -t, \phi)} \quad (31)$$

As an example, Fig. 29 shows the elements contributing to the  $\pi^0$  background subtraction, as were evaluated for the extraction of the TSA in the CLAS eg1-dvcs analysis, for two particular kinematic bins in  $(Q^2, x_B, -t)$ . Note that the impact on the final asymmetry of the background subtraction is quite small: an average effect of roughly 10%, relative to the value of the TSA at  $90^\circ$ , was estimated for this data set. In fact, what will impact the final asymmetries is not the size of the contamination itself, but the point-by-point difference of contamination for positive and negative target (or beam-target) polarization.

The proton-DVCS analysis of the eg1-dvcs  $\text{NH}_3$  dataset showed that a combination of optimized cuts on the exclusivity variables, designed to minimise the background, and the simulation- and data- based subtraction of Eq. 31 to remove the remaining contamination was a sound technique. In terms of systematics, the asymmetries were minimally affected even when the background estimation was artificially varied by 30%. This is important also because it shows how little this procedure depends on the Monte-Carlo model adopted.

## 10 Dilution factor

For both the nDVCS and  $en\pi^0$  final states, dilution factors are necessary to correct the experimental yields for the contribution from the scattering on the unpolarized nitrogen of  $\text{ND}_3$ . The

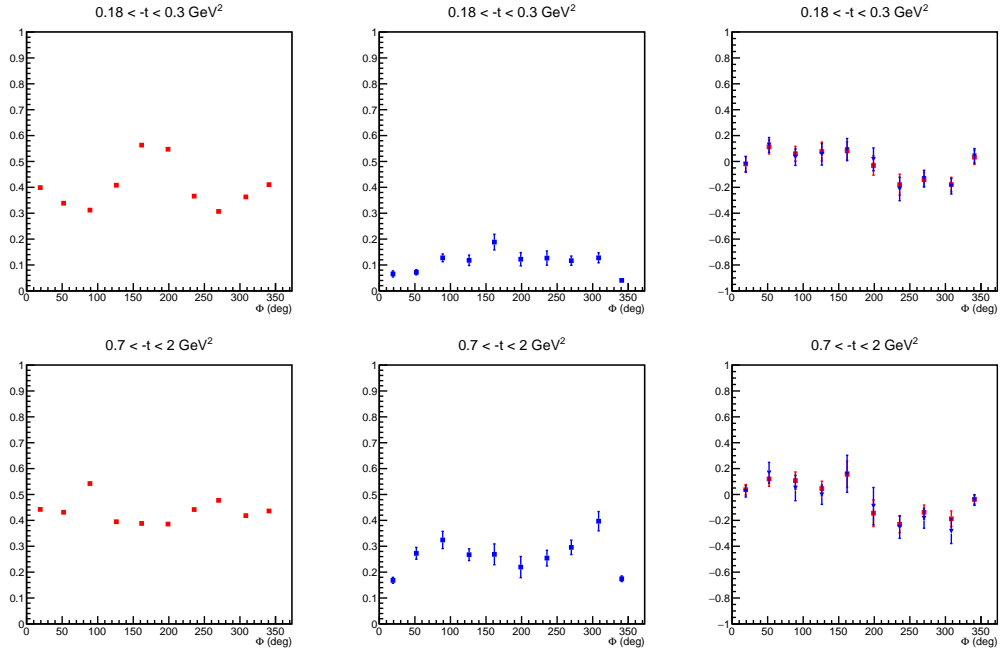


Figure 29: Plots from the proton-DVCS analysis of the eg1-DVCS CLAS dataset [14], for two different kinematic bins (top and bottom). Left: Acceptance ratio " $\frac{1\gamma}{2\gamma}$ "; middle:  $\pi^0$  contamination fraction; right: target-spin asymmetry before (red) and after (blue)  $\pi^0$  background subtraction.

dilution factor, that will be determined using data taken on ND<sub>3</sub> and on <sup>12</sup>C targets, is defined as

$$D_f = 1 - c \cdot \frac{N_{12C}}{N_{14ND_3}}. \quad (32)$$

Here,  $N_{12C}$  is the number of events, normalized by the corresponding Faraday-cup counts, obtained from a carbon target and surviving all of the nDVCS (or  $en\pi^0$ ) selection cuts, while  $N_{14ND_3}$  is the number of events, likewise normalized and passing the same series of cuts, originating from ND<sub>3</sub>. The factor  $c$  accounts for the different luminosities of the two sets of data, which also take into account the different areal densities of the materials present at the target level for the two kinds of runs (ND<sub>3</sub> in the numerator, <sup>12</sup>C in the denominator). For the eg1-dvcs experiment, it was found that the dilution factor, which, for pDVCS was determined to be around 0.9, does not display any sizeable dependence on any of the four kinematic variables describing the DVCS process. Adopting the same ratio as in eg1-dvcs, we estimate that acquiring ten times less events on <sup>12</sup>C than on ND<sub>3</sub> should provide a sufficient count rate of carbon events to estimate the dilution factor at a satisfactory level of precision. A value of about 0.8 was obtained in recent studies of exclusive channels on ND<sub>3</sub>, still using the eg1-dvcs dataset [48].

## 11 Accidentals in the CND

In order to evaluate the rate of accidentals being reconstructed as a false neutron in the CND in coincidence with an  $e\gamma$  event detected in CLAS12, GEMC simulations have been run in the following conditions [49, 8]: the primary electron has been generated going forward (to simulate the real hadronic event), plus 7500 other electrons have been thrown, distributed in a 124 ns window in bunches 4 ns apart, originating 10 cm upstream of the target. 7500 is approximately the number of beam electrons that would pass through our target in a 124 ns time window at the nominal CLAS12 luminosity. 124 ns is the typical time window of the DAQ expected for CLAS12, which corresponds to one event in CLAS12. These electrons then interact with the target itself, producing an electromagnetic and hadronic background hitting the neutron detector. The simulations were produced twice, using two different "physics lists" from GEANT4: electromagnetic plus hadronic processes ("EM-HAD"), and electromagnetic only (EM). The output of the simulations has been analyzed using the CND neutron-reconstruction algorithm. For each event, we selected the hit with the shortest time of flight which had a deposited energy above our chosen threshold (2 MeV) and below the maximum allowed time (9 ns). The reference time was chosen as that corresponding to the central beam bunch. Given the tight timing cuts that are imposed when reconstructing neutrons in the CND, we estimate that only slow neutrons ( $p \sim 0.2$  GeV) from the previous bunch or photons from the following bunch could be accidentally registered as originating from the bunch in question. The momentum of the chosen particle is reconstructed assuming that it is a neutron, and cuts are applied on its momentum ( $p_{min} = 0.2$  GeV/c) and on  $\beta$  ( $\beta < 0.95$ ). Since previous simulations showed us that real neutrons should only produce at most one hit in one of the three layers of the CND, particles which had a second hit in another layer along the same trajectory were also removed. Figure 30 shows the energy distribution of the background hits in the CND before any cuts are applied for the EM (top) and EM-HAD (bottom) cases. The latter has a more important tail at higher energies.

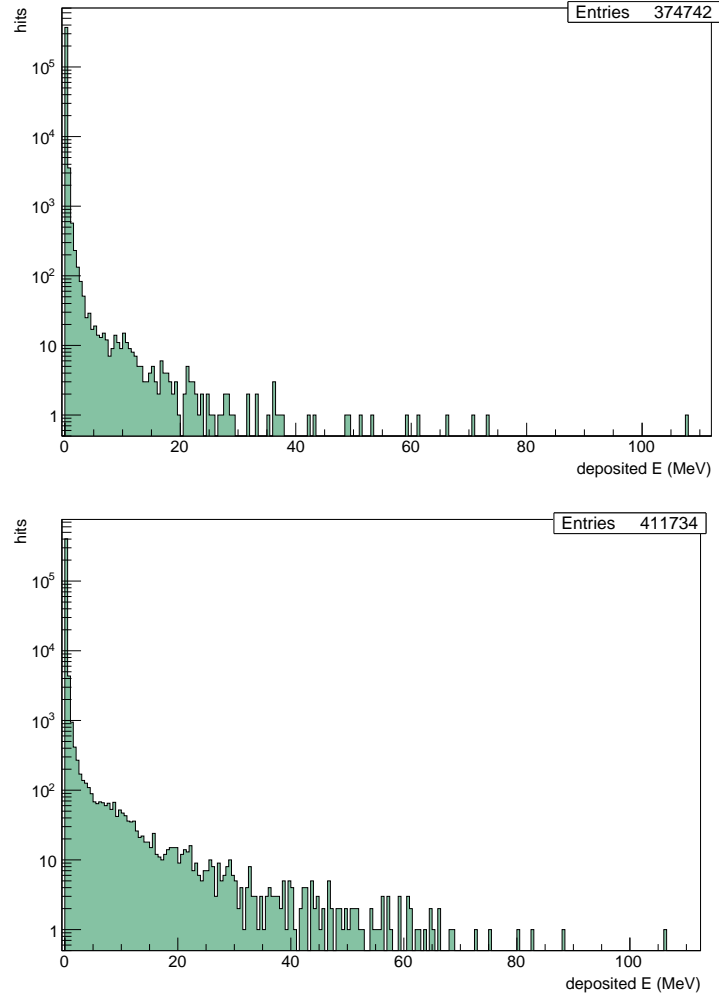


Figure 30: Energy deposited by the background hits in the CND, before cuts, as obtained with GEMC plus the EM physics list (top) and the EM-HAD one (bottom).

The resulting probabilities that an event has a hit which passes the CND cuts are 0.0012 for the EM case and 0.01 for the EM-HAD case. Care must be taken in considering the EM-HAD probability, as there can be, on the one hand, double counting due to some of the simulated hadronic events producing actual triggers in CLAS12, and, on the other hand, uncertainties due to the GEANT4 parametrization of the physics list. The GEMC simulation of the whole CLAS12 and the full reconstruction software would be necessary to provide a more accurate estimate, but neither are available yet. The 0.01 of the EM-HAD case must therefore be regarded as a conservative upper limit. These hits can mimic a fake n-DVCS event by accidental coincidence with hadronic events where an electron and an energetic photon ( $E_\gamma > 2$  GeV) are detected in the forward part of CLAS12. The  $e\gamma$  rate was estimated to be at most 50 Hz: the dominant process at play here is SIDIS with production of a  $\pi^0$ ; the rate for such a process was estimated in [50] to be of 9 Hz (obtained by taking into account the factor of 20 greater luminosity in the present experiment). Given that various kinematic cuts and the detection of both photons were required to produce that figure, we take a very conservative approach, assuming a rate for such events of the order of 50 Hz. This yields an accidental coincidence rate of the order of 0.06 Hz for the EM physics list, and 0.5 Hz for the EM+HAD physics list. These figures will be further reduced once the exclusivity cuts (Section 8.1) will be applied, and will be therefore safely smaller than the expected rate for real  $en\gamma$  events, which was estimated, with our event generators and FastMC, to be of 1 Hz for the present experiment.

## 12 Projected results

A GPD-based event generator for DVCS-BH on a deuterium target was run, assuming a luminosity of  $3/20 \cdot 10^{35} \text{ cm}^{-2} \text{ s}^{-1}$  (where the factor 3/20 accounts for the ratio of polarized neutrons to the total nucleons in ND<sub>3</sub>) and a beam time of 50 days. The output of the generator was fed to the CLAS12 Fast-MC code, which included acceptance and resolution effects for CLAS12 and the CND. An additional factor of 10% was also applied to mimick the efficiency of the CND for neutrons<sup>7</sup>. nDVCS exclusivity cuts were then applied. This way, the expected yields for the  $en\gamma(p)$  events produced on the ND<sub>3</sub> target were obtained. The kinematic space (in  $Q^2, x_B, -t, \phi$ ) available with the acceptance of the CLAS12+CND setup was divided into the same 4-dimensional grid that was used for the unpolarized nDVCS proposal:

- 4 bins in  $Q^2$ , the limits of which are: 1, 2, 3.5, 5, 10 (GeV)<sup>2</sup>;
- 4 bins in  $x_B$ , the limits of which are: 0.05, 0.15, 0.3, 0.45, 0.7;
- 4 bins in  $-t$ , the limits of which are: 0, 0.2, 0.5, 0.8, 1.2 (GeV)<sup>2</sup>;
- 12 bins in  $\phi$ .

The central kinematics for each bin were computed as weighted averages over the reconstructed events. The target-spin asymmetry and the double-spin asymmetry were then calculated as a function of  $\phi$  using the VGG model (with input parameters  $J_u = 0.3$  and  $J_d = 0.1$ ) for each of the  $(Q^2, x_B, -t)$  bins that are kinematically allowed. Statistical errors were then

---

<sup>7</sup>Actually, this factor was adopted globally for ALL neutrons, even those falling within the EC acceptance. Given that the EC should have higher neutron efficiency than the CND, by at least a factor of 2, the projections for the count rates shown here are slightly pessimistic.

obtained for these asymmetries using the approximated formula:

$$\sigma_A = \frac{1}{P} \cdot \frac{\sqrt{1 - P^2 \cdot A^2}}{\sqrt{N}}. \quad (33)$$

where  $P$  is the polarization (and it is therefore equal to the target polarization for neutrons,  $P_t$ , for the TSA case, and to the product of beam and target polarizations,  $P_b P_t$ , for the DSA case), and  $N$  is the expected yield in each 4-dimensional bin (Figs. 43 and 44).

The resulting asymmetries with the associated expected error bars are shown in Figs. 31 and 32.

For reference, the 4-dimensional acceptances obtained with the simulation are shown in Figs. 45 and 46.

## 13 Extraction of Compton Form Factors

The three sets of projected asymmetries (BSA from [8], shown in Fig. 33, TSA and DSA from this work, Figs. 31 and 32, respectively) for all kinematic bins were processed using the fitting procedure described in Section 4 to extract the Compton Form Factors of the neutron. In the adopted version of the fitter code,  $\tilde{E}_{Im}(n)$  is set to zero, as  $\tilde{E}(n)$  is assumed to be purely real - it is parametrized in the VGG model by the pion pole ( $1/(t - m_\pi^2)$ ). Thus, seven out of the eight real and imaginary parts of the CFFs are left as free parameters in the fit. A loose bound on the parameters is also applied, limiting them within the interval given by  $\pm 5 \cdot \text{VGG}$ , where "VGG" stands for the prediction of the VGG model for the value of the CFF.

The results for the 7 neutron CFFs are shown in Figs. 34-40, as a function of  $-t$ , and for each bin in  $Q^2$  and  $x_B$ . The blue points are the CFFs resulting from the fits with their asymmetric error bars, which reflect both the statistical precision of the fitted observables and their sensitivity to that particular CFFs. Only results for which both halves of the error bars are non zero, and therefore the fits have properly converged for that CFF, are included here.

The CFFs which will be obtained with more precision and for most of the kinematic points that will be covered by the proposed experiment are  $H_{Im}(n)$  and  $E_{Im}(n)$ . This is to be expected, since the TSA and the BSA are most sensitive to these two CFFs. A quite good sensitivity to  $\tilde{E}_{Re}(n)$  seems possible in a wide kinematics range.  $\tilde{H}_{Re}(n)$  will also be obtained in most of the kinematic bins, thanks to the peculiar sensitivity of the DSA for this CFF.  $\tilde{H}_{Im}(n)$  will be well extracted only in the low  $Q^2$ - $x_B$  kinematics. Finally, it appears that these data will not be able to provide much information on  $E_{Re}(n)$ .

## 14 Flavor separation of CFFs

In order to convey the impact of this experiment on the JLab GPD program, an example of model-independent flavor separation of CFFs, which our experiment will make possible for the first time, is shown in Figs. 41 and Figs. 42. Here, the CFFs  $H_{Im}$  (Fig. 41) and  $E_{Im}$  (Fig. 42) are shown, for two different bins in  $Q^2$ - $x_B$  (left-right), as a function of  $-t$ , for the two nucleons (top, where the proton is represented in black and the neutron in red) and for the two quark flavors (bottom, where black represents  $u$  and red  $d$ ). These figures has been produced using the proton CFFs that were extracted combining all the projected results for the

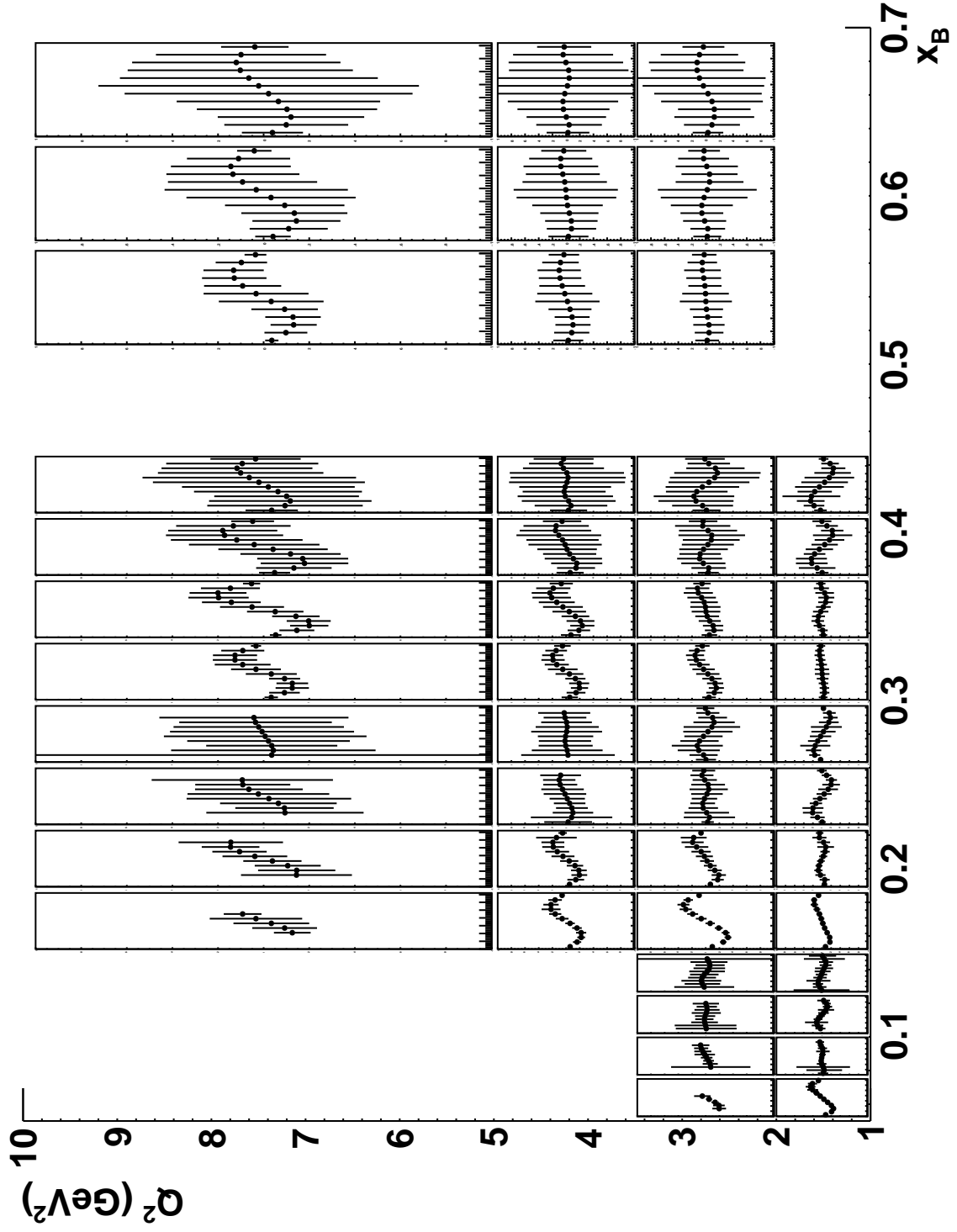


Figure 31: Projected target-spin asymmetry. The y-scale range, common to all bins, is  $(-1;1)$ .



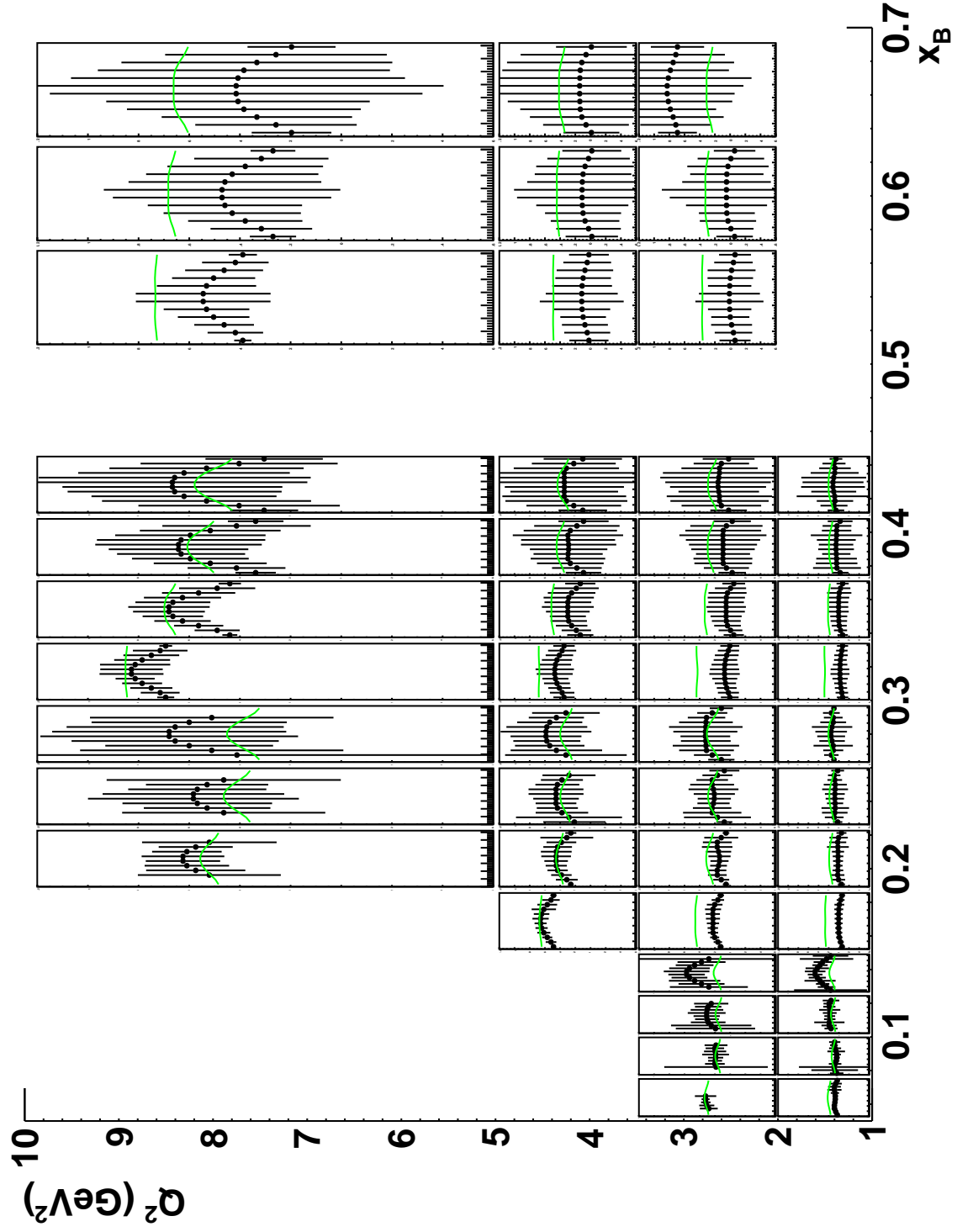


Figure 32: Projected double-spin asymmetry, compared with the BH (green lines), calculated at the average kinematics of each bin. The y-scale range, common to all bins, is -0.6-1.2.

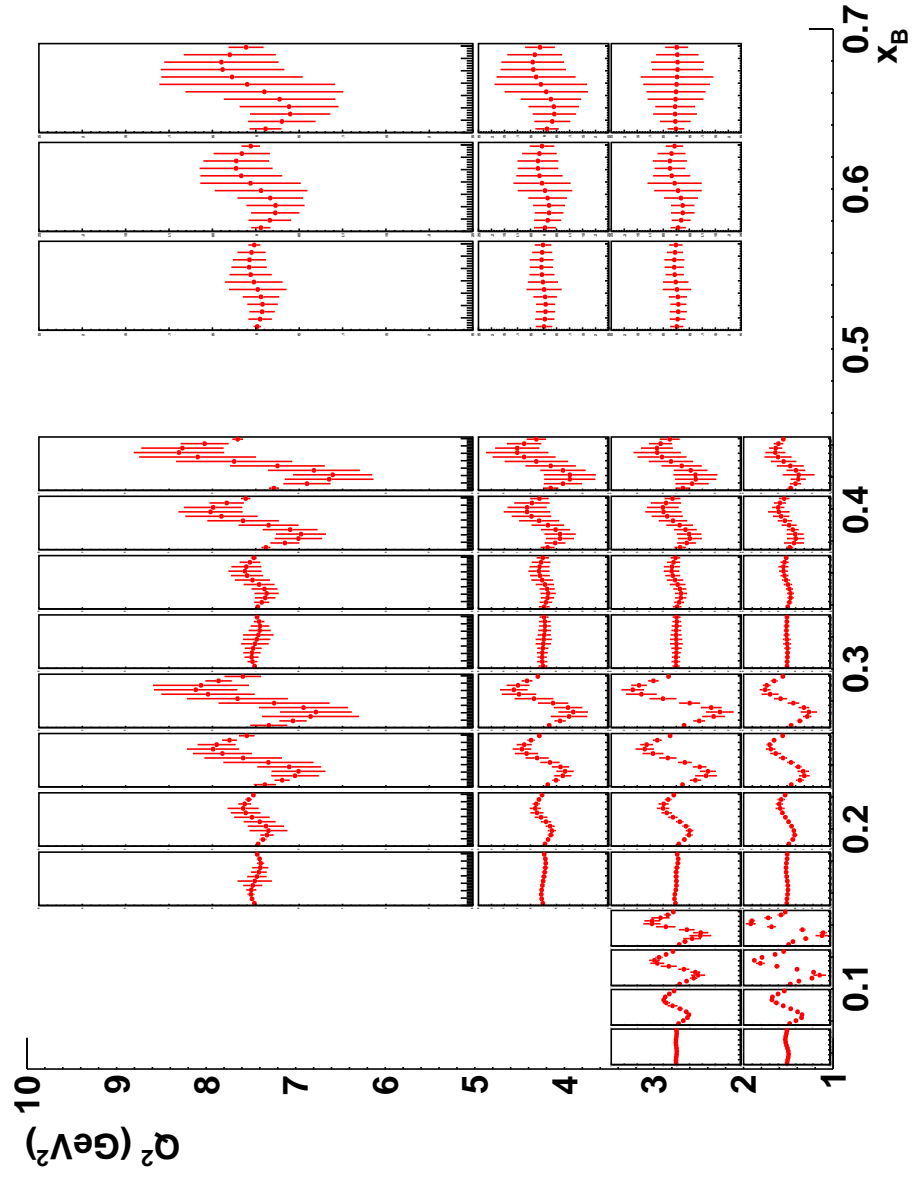


Figure 33: Projected beam-spin asymmetry, as will be obtained from experiment E12-11-003 [8]. The y-scale range, common to all bins, is -0.25-0.25.

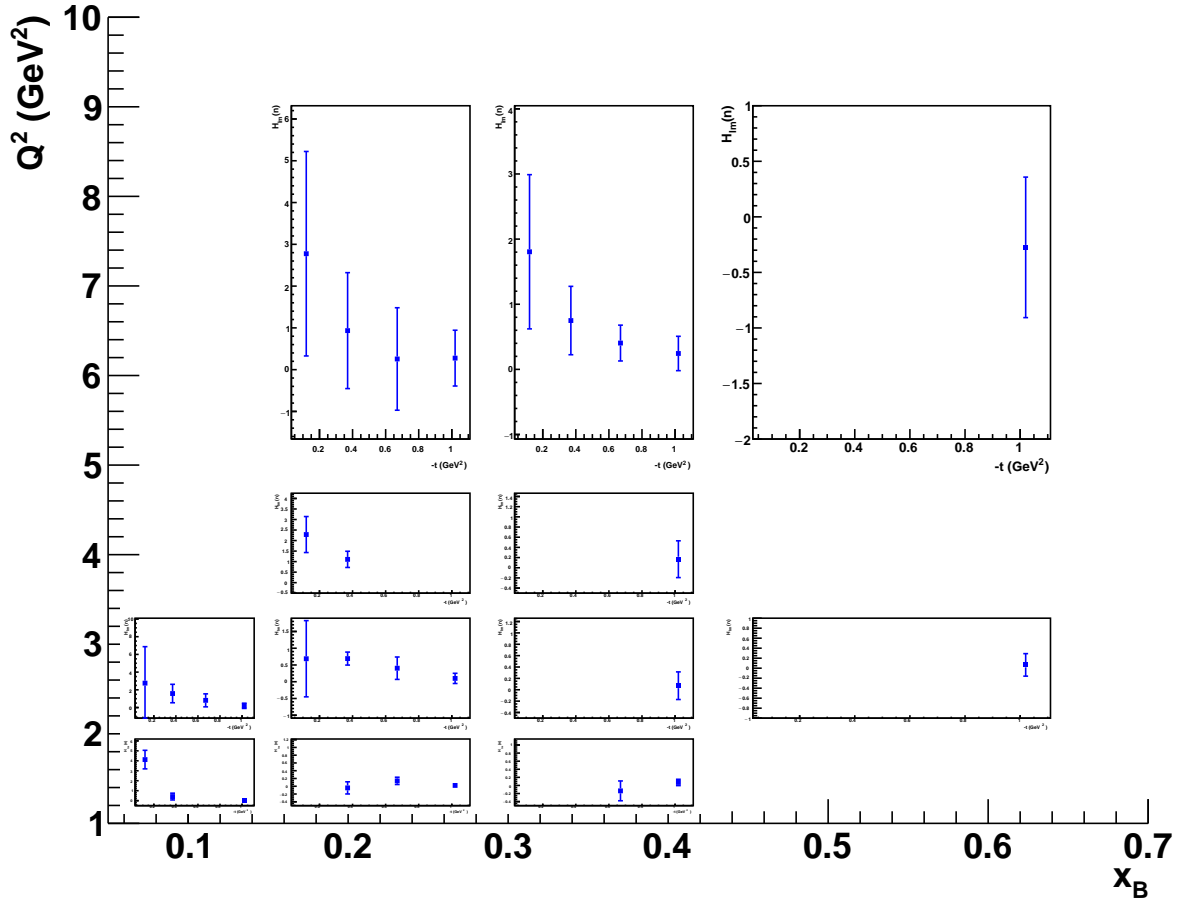


Figure 34:  $H_{Im}(n)$  as a function of  $-t$ , for each bin in  $Q^2$  and  $x_B$ .

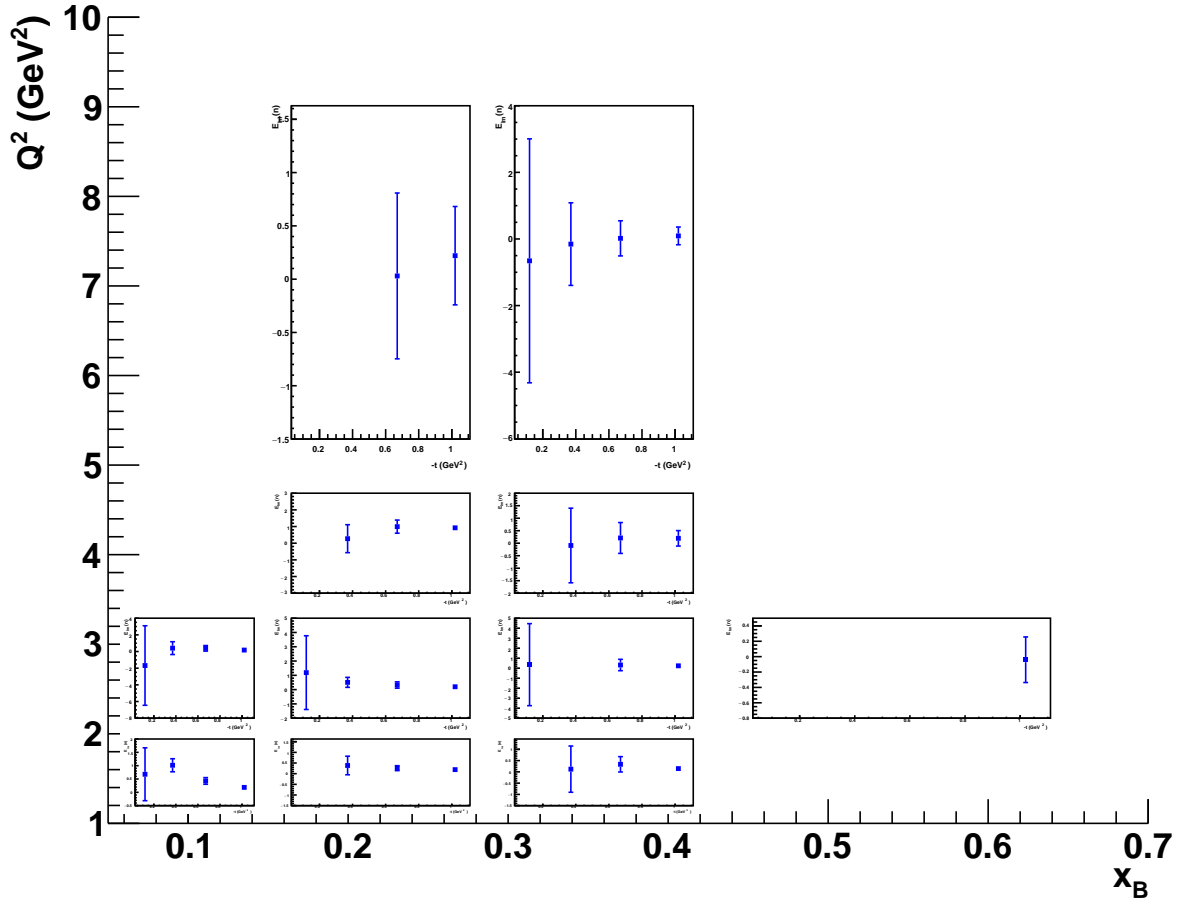


Figure 35:  $E_{Im}(n)$  as a function of  $-t$ , for each bin in  $Q^2$  and  $x_B$ .

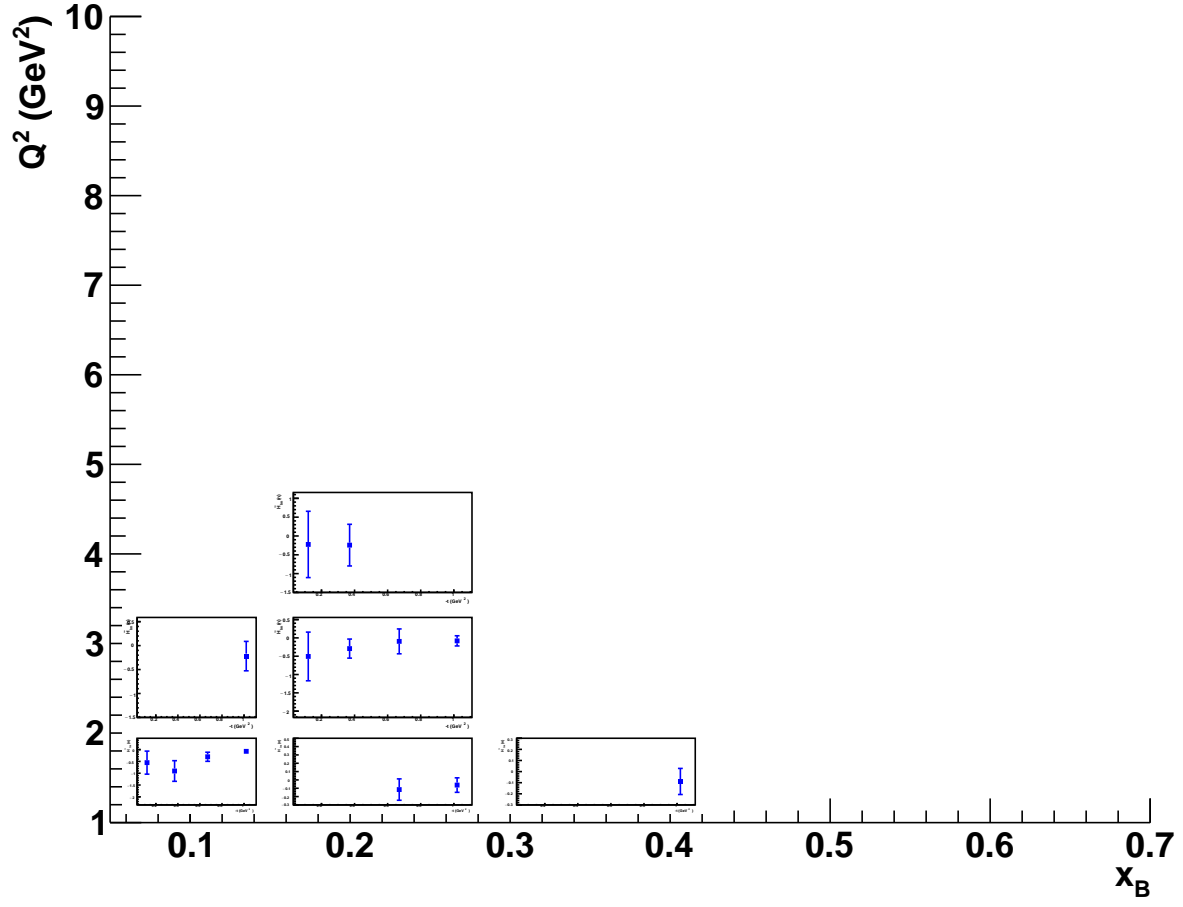


Figure 36:  $\tilde{H}_{Im}(n)$  as a function of  $-t$ , for each bin in  $Q^2$  and  $x_B$ .

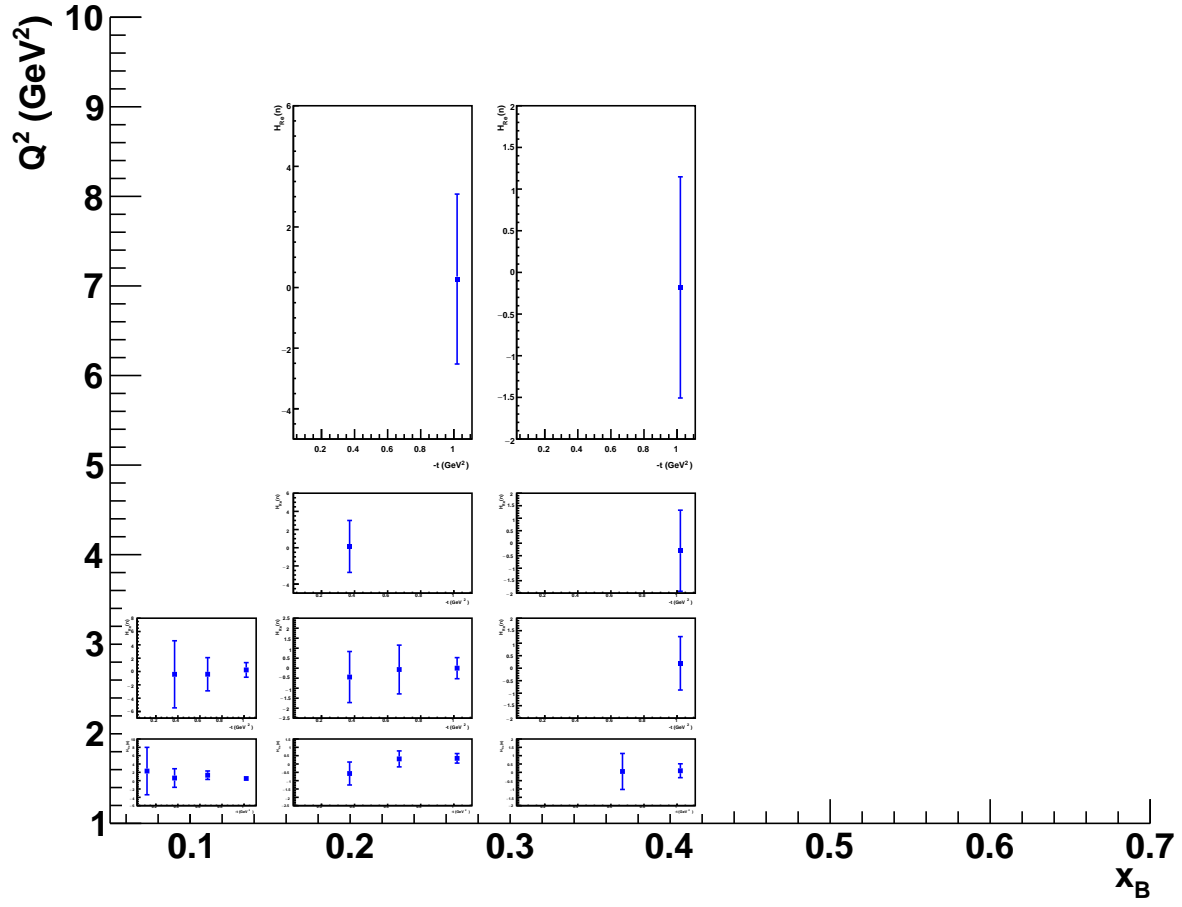


Figure 37:  $H_{Re}(n)$  as a function of  $-t$ , for each bin in  $Q^2$  and  $x_B$ .

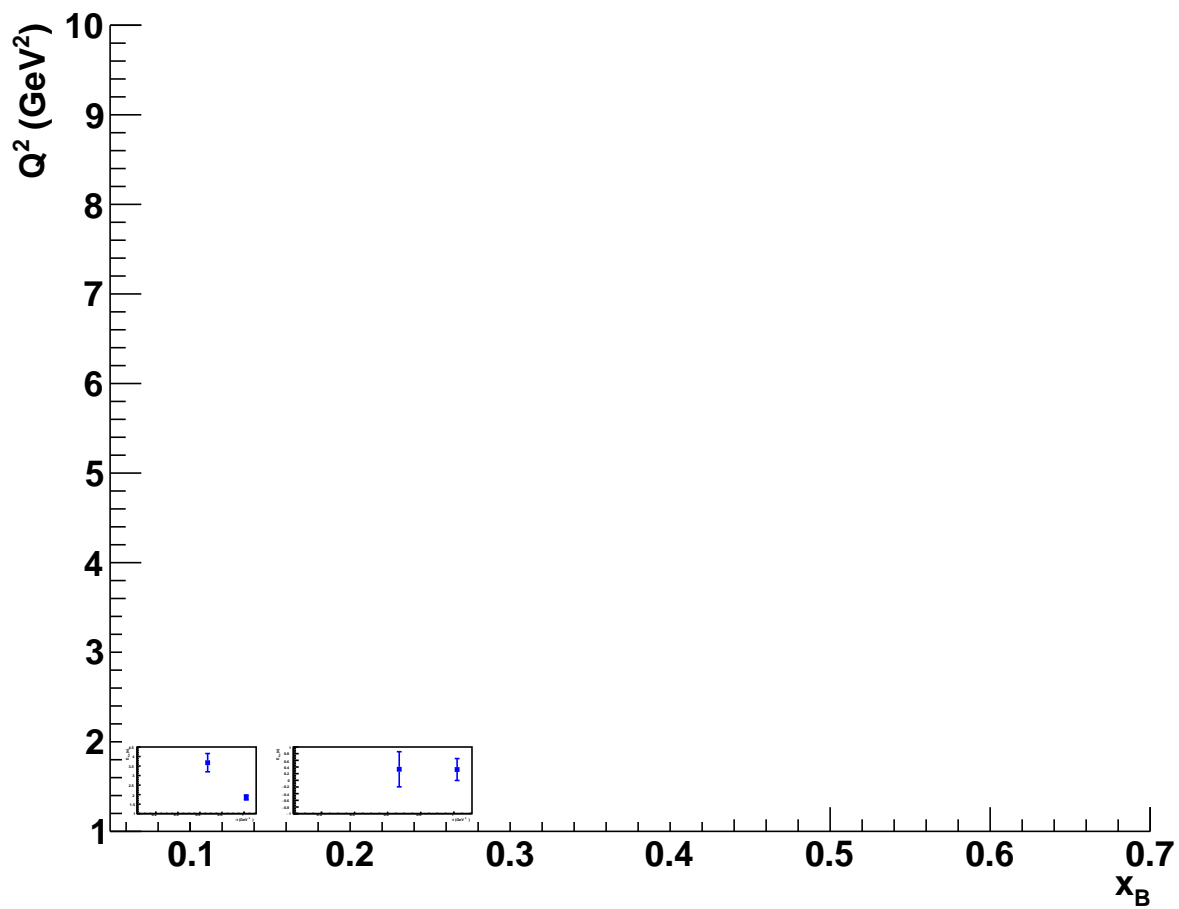


Figure 38:  $E_{Re}(n)$  as a function of  $-t$ , for each bin in  $Q^2$  and  $x_B$ .

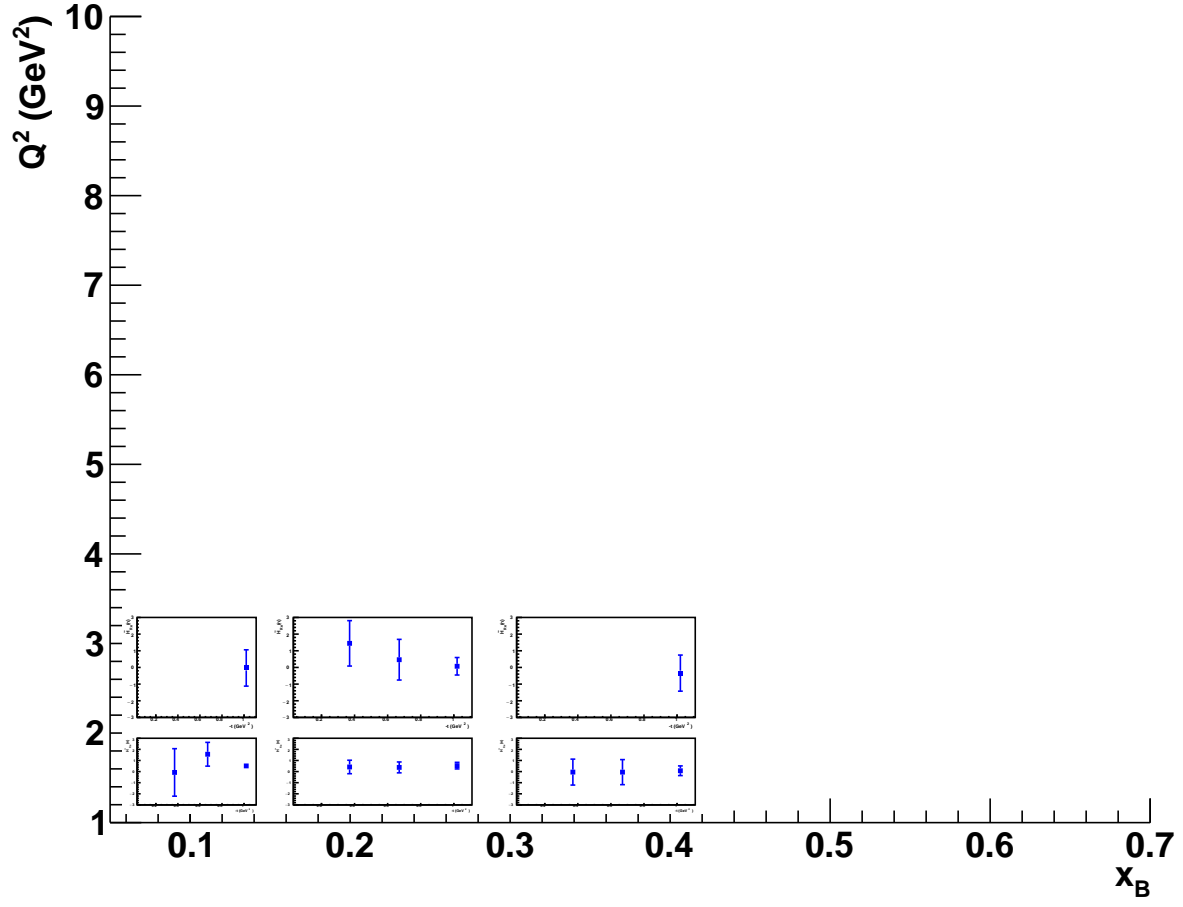


Figure 39:  $\tilde{H}_{Re}(n)$  as a function of  $-t$ , for each bin in  $Q^2$  and  $x_B$ .



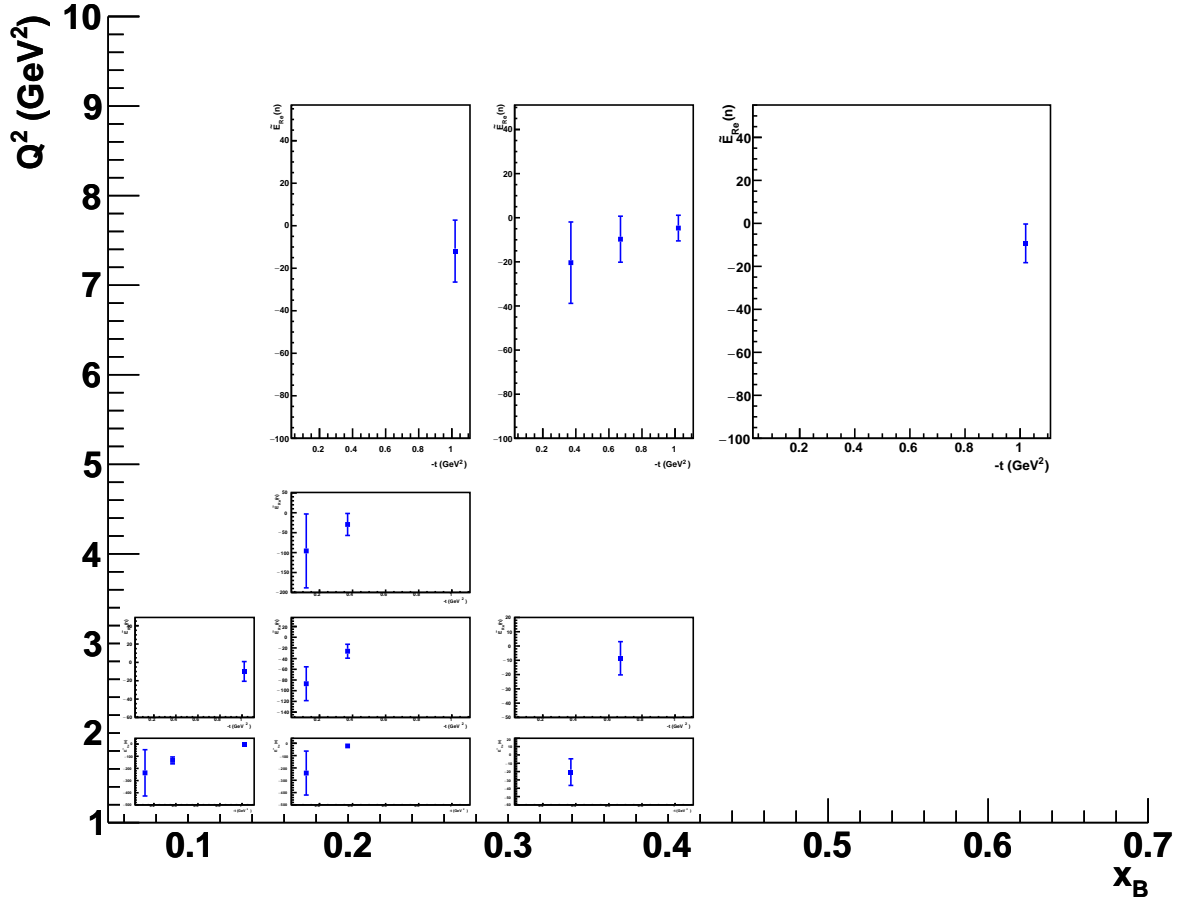


Figure 40:  $\tilde{E}_{Re}(n)$  as a function of  $-t$ , for each bin in  $Q^2$  and  $x_B$ .

pDVCS asymmetries that will be measured with CLAS12 [11], with the neutron CFF that were shown in Section 13 <sup>8</sup>.

The flavor separation of the CFFs will represent a major step forward towards the unraveling of the contribution of the quarks' angular momentum to the total nucleon spin via Ji's sum rule [2]:

$$\sum_q \int_{-1}^{+1} dx x [H^q(x, \xi, t=0) + E^q(x, \xi, t=0)] = 2 J_{quarks}. \quad (34)$$

## 15 Systematic uncertainties

The goal of this experiment is to extract target and double-spin asymmetries, which are ratios of polarized cross sections. In the ratio, polarization-independent terms, such as acceptances, efficiencies, radiative corrections and luminosity, cancel out to a first approximation<sup>9</sup>. Remaining effects could come from the quantities entering in the asymmetry definitions, namely the procedure to evaluate the counts  $N^{+(-)}$ , the dilution factor, the  $\pi^0$  contamination, as well as the beam and target polarizations.

Analyses performed at 6 GeV [15, 14] showed that the biggest contributor to the overall systematic uncertainty is the selection of exclusivity cuts adopted to identify DVCS events and the corresponding counts  $N^{+(-)}$ . This factor contributed about 10% (this and the following percentages for systematics are defined relatively to the average value of the TSA at 90°) to the total systematics uncertainty.

Another source of uncertainty will be the  $\pi^0$  background estimation, which will depend on the accuracy of the description of the detector acceptance and efficiency and on the model used in the Monte-Carlo simulation to describe the  $en\pi^0(p)$  reaction (see Eq. 32). In order to account for this latter effect, 6-GeV analyses, performed on data taken on a polarized  $\text{NH}_3$  target during the eg1-dvcs experiment [15, 14], evaluated this systematic by varying the contribution of the calculated background by  $\pm 30\%$  (Section 9), and extracting the final asymmetries in correspondence with this increased/decreased background. The total effect turned out to be 4%, and a similar estimation can be assumed for the present experiment on  $\text{ND}_3$ .

While acceptance effects are expected to cancel in asymmetries, a residual effect could emerge due to the strong variations of the cross section inside the finite-size bins, that can lead, in principle, to a non-exact cancellation of acceptance effects from the numerator and the denominator. Such an acceptance effect has been estimated to bring an additional 1% systematic error.

To evaluate the systematic uncertainties linked to the dilution factor determination, in the aforementioned eg1-dvcs pDVCS analysis the asymmetries were computed two more times,

---

<sup>8</sup>In the case of  $E_{Im}$ , the figure must be taken only as an indication of the potential of the present experiment. In fact the measurement of  $E_{Im}(p)$ , and its uncertainties, depend strongly on the feasibility of the conditionally approved pDVCS experiment with transversely-polarized target [25].

<sup>9</sup>Afanasev *et al.* [52] have computed the radiative corrections for the DVCS and BH processes on for CLAS kinematics. It was found that, given the strict kinematic cuts adopted to select the final state, the undetected radiated photon can only have small energies. In this case, therefore, the main contribution to the radiative correction comes from spin-independent soft-photon emission that does not affect the polarization observables. The approximation of negligible contribution from the radiative corrections to the BSA, TSA and DSA, compared to the size of the asymmetries, was estimated to be valid at the 0.1% level [52].

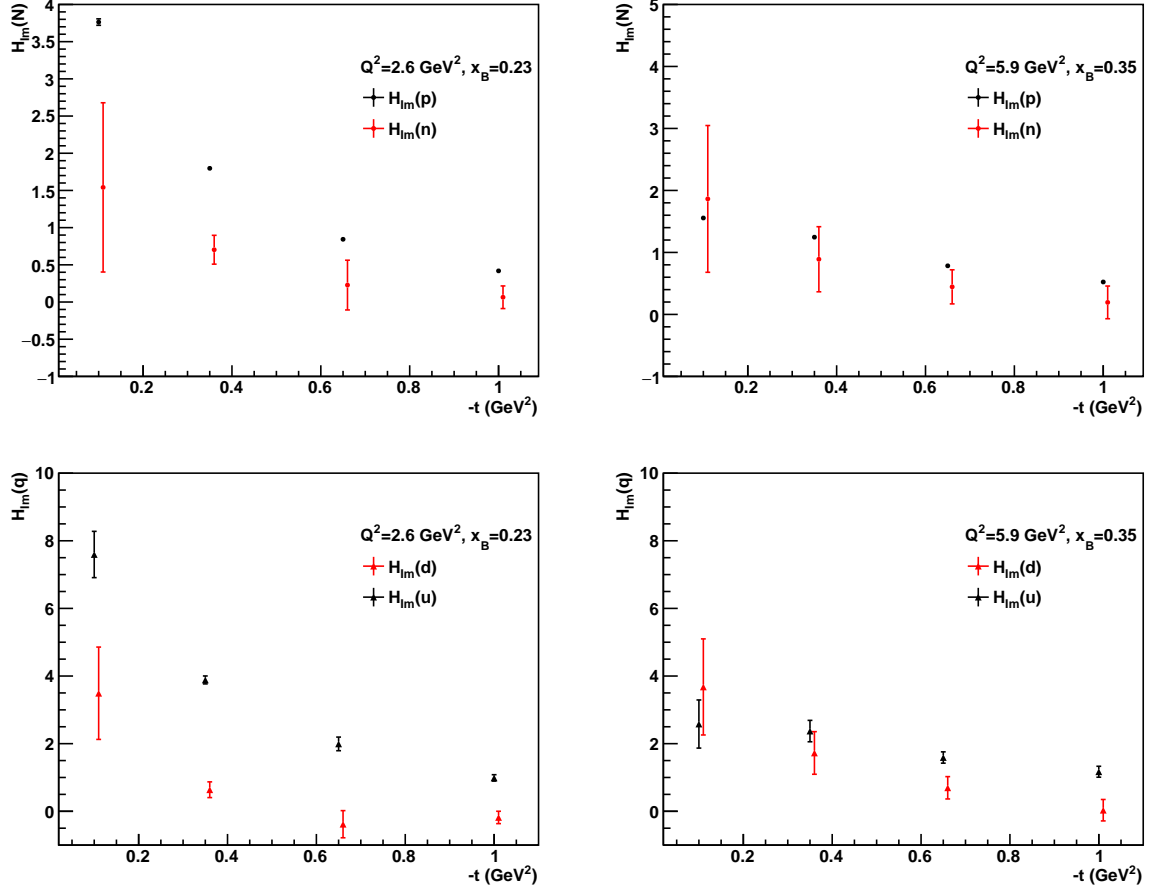


Figure 41: Top:  $H_{Im}(p)$  (black), extracted from the projection for the approved and conditionally-approved proton-DVCS CLAS12 experiments, and  $H_{Im}(n)$  (red), obtained from the projections of the proposed experiment, as a function of  $-t$ . Bottom: Quark-flavor separated  $H_{Im}$ , black for  $u$  and red for  $d$ . Two different bins in  $Q^2$ - $x_B$ , indicated in the legends, are shown in the left and right columns.

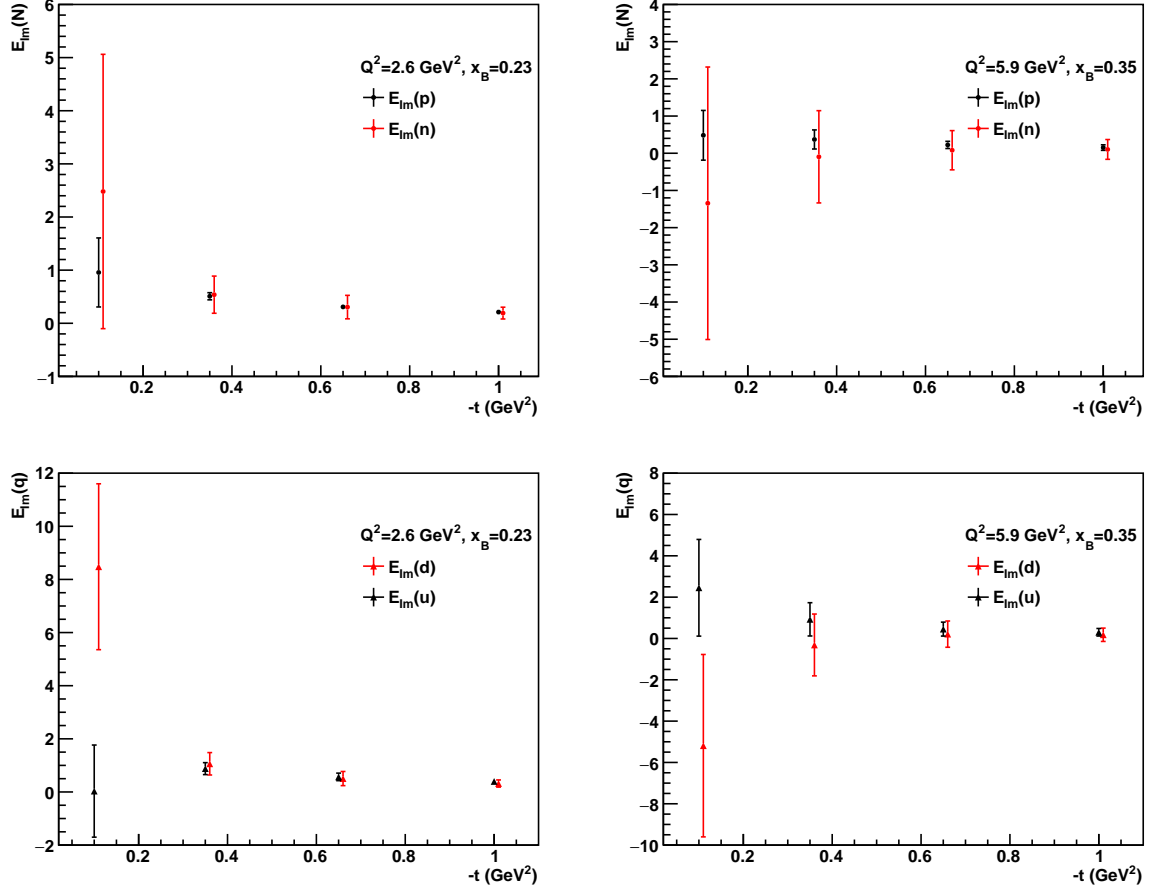


Figure 42: Top:  $E_{Im}(p)$  (black), extracted from the projection for the approved and conditionally-approved proton-DVCS CLAS12 experiments, and  $E_{Im}(n)$  (red), obtained from the projections of the proposed experiment, as a function of  $-t$ . Bottom: Quark-flavor separated  $E_{Im}$ , black for  $u$  and red for  $d$ . Two different bins in  $Q^2$ - $x_B$ , indicated in the legends, are shown in the left and right columns.

Source of error	Systematic uncertainty
Channel selection cuts	10%
Beam and target polarization	3%-4%
$\pi^0$ contamination	4%
Acceptance	1%
Dilution factor	3%
Accidentals	2%
Radiative corrections	Negligible
Total	12%

Table 2: Expected systematic uncertainties on the proposed measurement.

taking two different values of the dilution factor:  $D_f + \Delta(D_f)$  and  $D_f - \Delta(D_f)$ , where  $\Delta(D_f)$  is the statistical error that was estimated on this quantity. The resulting systematic uncertainties were found to be below the percent level. While studying the systematics on the exclusivity cuts, it was observed that changing the exclusivity cuts induces a variation of the dilution factors much bigger than the variations within the statistical errors described above. It was therefore decided, in order to avoid double-counting and therefore overestimation of systematics, to remove the contribution from the dilution factor computed according to its errors from the total systematic uncertainty. For this proposal, instead, a conservative estimate of the systematic uncertainty on the dilution factor of the order of 3%, consistent with previous assumptions [53], is assumed.

An additional 2% systematic effect is included in the total budget to account for the possible misidentification of neutrons due to accidental coincidences (Section 11.)

Finally, uncertainties in the knowledge of the beam and target polarizations (extracted, respectively, via Møller polarimetry measurements and via the NMR system) will propagate into the asymmetry measurements, and are expected to lead to contributions of, respectively, 3% and 4%.

A summary of the systematic uncertainties can be found in Table 2. The total systematic uncertainty will be of the order of 12%, averaged over all the kinematic bins (the  $\pi^0$ -background uncertainty will actually vary depending on the bin).

## 16 Beam-time request

We request 50 days of production running on the  $^{14}\text{ND}_3$  target with an 11-GeV polarized electron beam, at 10 nA of current. Our experiment will share beam time with the other experiments which are part of Run Group Cb. In order to acquire the roughly 10% of counts on  $^{12}\text{C}$  that are necessary to estimate the dilution factor (Section 10) and to remove the nuclear background when studying the exclusivity cuts (Section 8.1), and given the maximum tolerable luminosity of CLAS12 of  $10^{35} \text{ cm}^{-2}\text{s}^{-1}$ , we request 5 additional days of running on a 2-cm-long  $^{12}\text{C}$  target, also with a beam intensity of 10 nA. Four days will be spent, with and without beam, in target-related operation, as explained in Section 6.1.3. Including 1 day of Moeller runs to monitor the beam polarization (assuming a one-hour long run per calendar day) the

Production data taking at $10^{35} \text{ cm}^{-2}\text{s}^{-1}$ on $\text{ND}_3$	50 days
Target work	4 days
Production data taking on $^{12}\text{C}$ target	5 days
Moeller polarimeter runs	1 day
Total beam time request	60 days

Table 3: Beam-time request.

whole experiment will take 60 PAC days for completion.

## 17 Conclusions

Our knowledge of the three-dimensional structure of the nucleon has become richer in the last few years thanks to the introduction of the formalism of the Generalized Parton Distributions and to the subsequent wealth of experimental results on Deeply Virtual Compton Scattering which have recently become available. After the pioneering experimental results on DVCS, which raised the interest in this reaction as a means to achieve a tomographic description of the nucleon, it became evident, thanks to the analysis of the second generation of proton-DVCS dedicated experiments and to the advancement in the theory and phenomenology of GPDs, how only the combined measurement of several DVCS observables in a vast kinematic space can allow one to disentangle the contributions of the various GPDs and their complex kinematic dependences. While our knowledge of the three-dimensional structure of the proton is progressing considerably - the first attempts at its tomographic description have recently been made thanks to CLAS data taken at 6 GeV [14, 22], and a vast experimental program of pDVCS is planned for JLab at 12 GeV - neutron GPDs remain a mostly virgin field at this stage. The importance of extracting neutron CFFs is paramount if we want to ultimately perform a flavor decomposition of the GPDs. We propose here to make the first ever nDVCS measurements of spin observables, target- and double-spin asymmetries, with a polarized target. We view the experiment as complementary to E12-11-003, which will measure the beam-spin asymmetries for nDVCS at the same kinematic points, and which is currently listed as a "high-impact" 12-GeV experiment. The detector system will not require additions nor upgrades with respect to components which are currently under construction or already completed. The polarized target is already being developed and will be used also for other CLAS12 experiments. Having extracted both the TSA and DSA will allow us to extract, fitting them together with the BSA from E12-11-00, various neutron Compton Form Factors in a model-independent way. Quark-flavor separation will be obtained by the linear combination of these neutron CFFs with the proton CFFs extracted from the pDVCS CLAS12 experiments.

## A Appendix: Count rates and acceptances

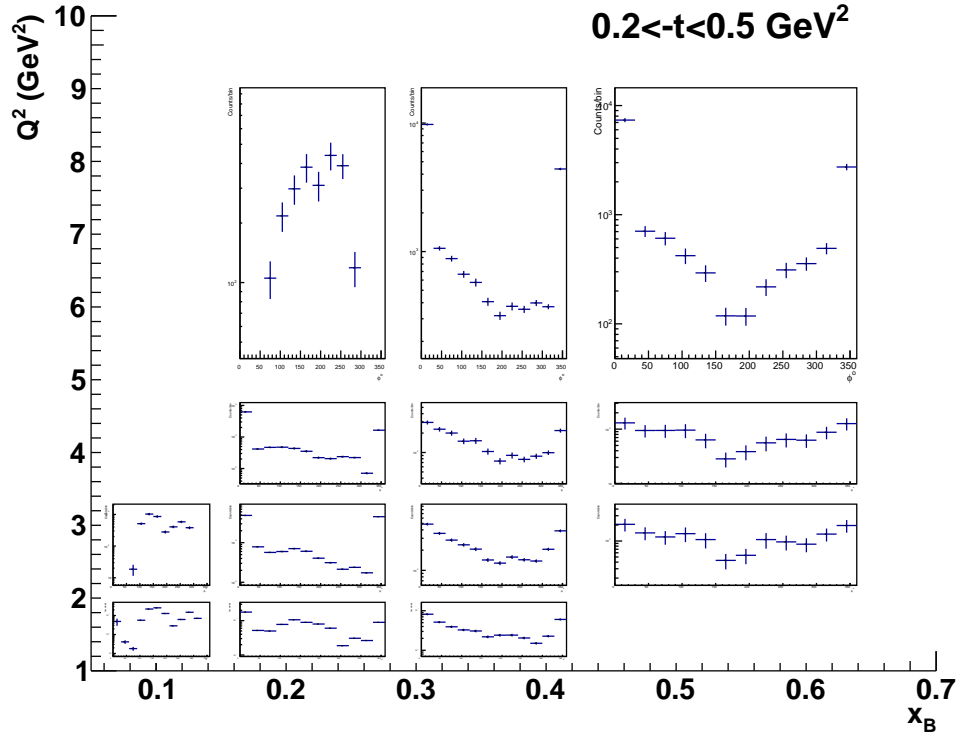
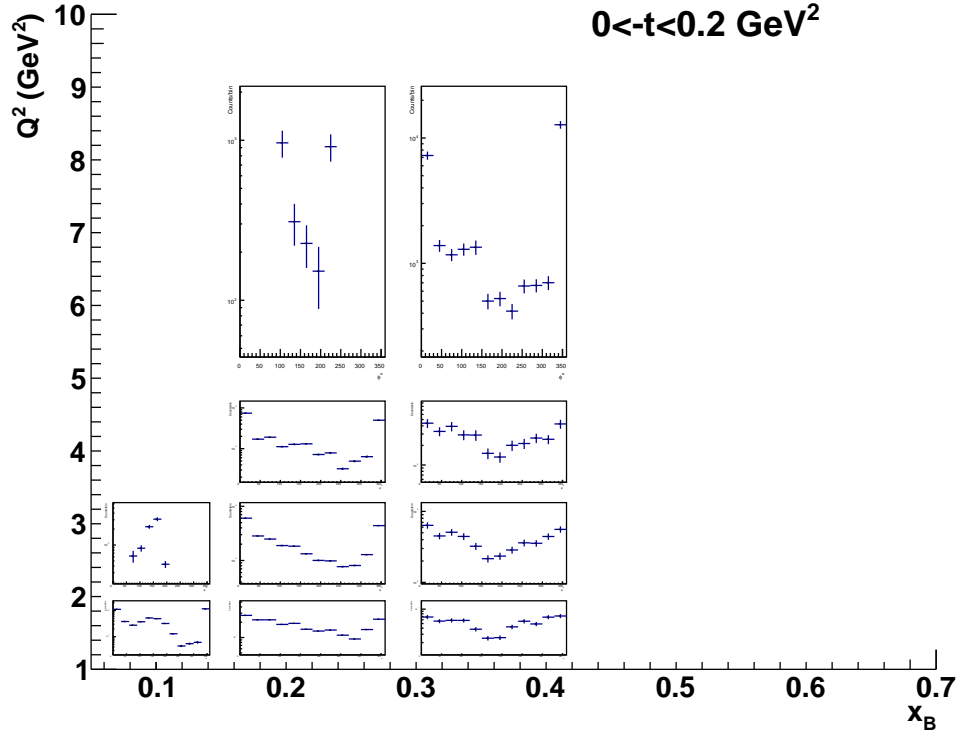


Figure 43: Expected count rates for the nDVCS channel:  $0. < -t < 0.2 \text{ GeV}^2$  (top) and  $0.2 < -t < 0.5 \text{ GeV}^2$  (bottom).

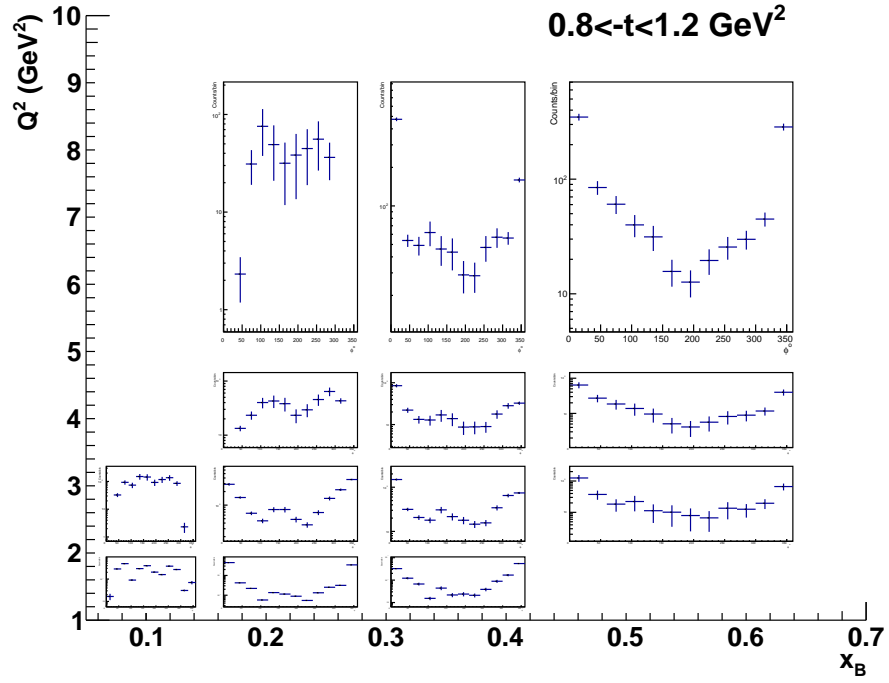
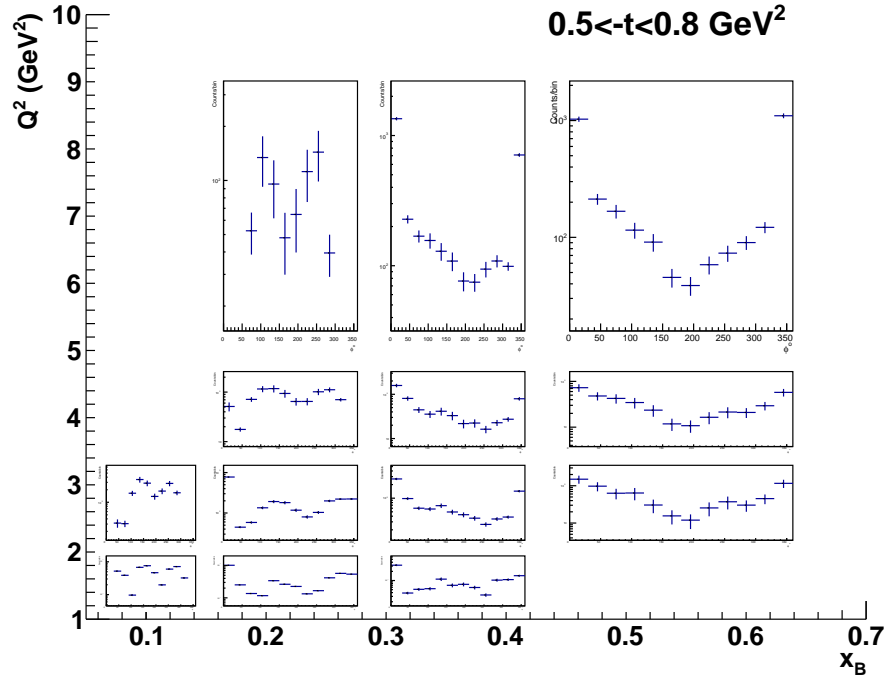


Figure 44: Expected count rates for the nDVCS channel:  $0.5 < -t < 0.8 \text{ GeV}^2$  (top) and  $0.8 < -t < 1.2 \text{ GeV}^2$  (bottom).



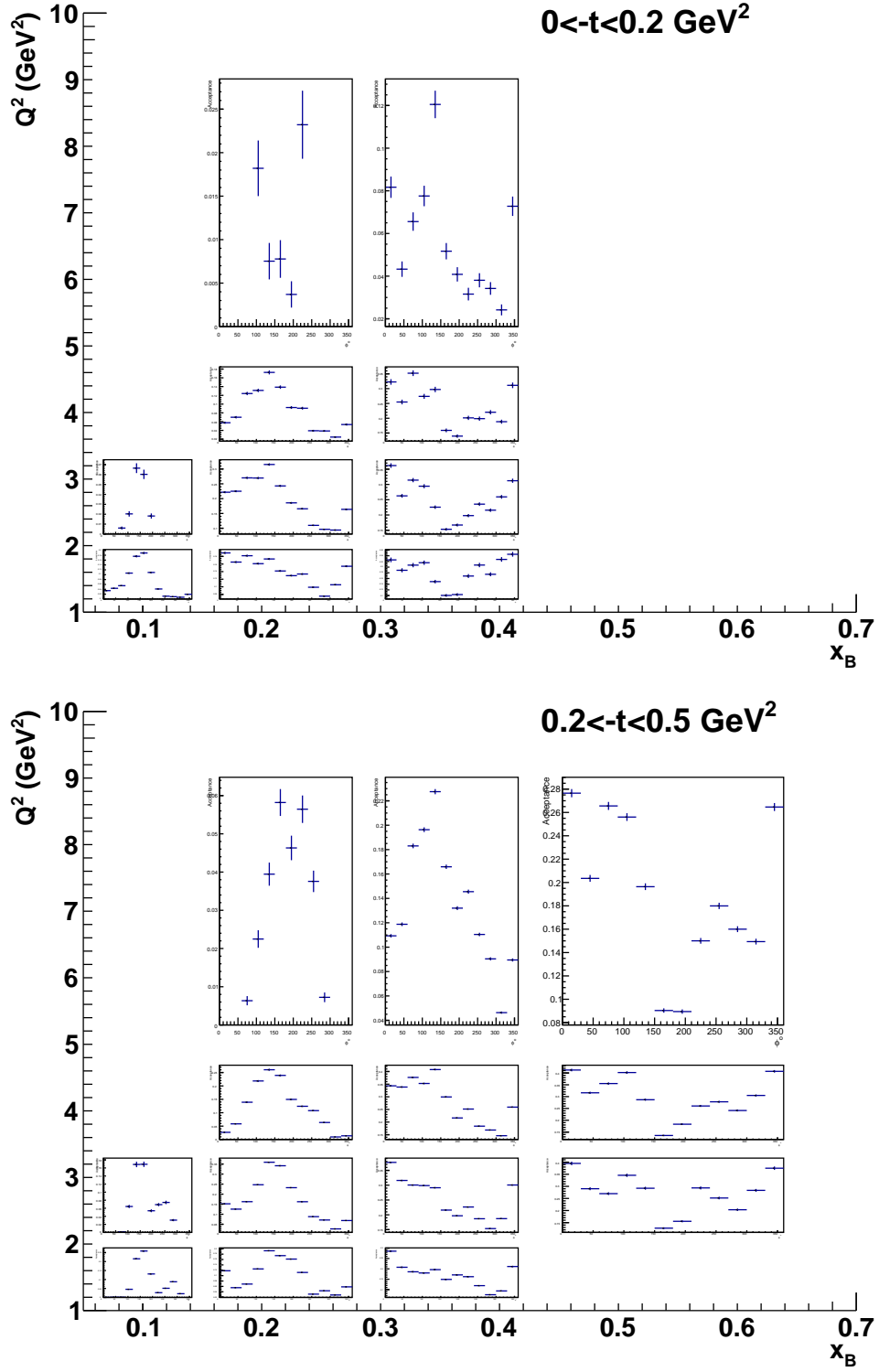


Figure 45: Expected acceptances, including the 10% of efficiency for the CND, for the nDVCS channel:  $0. < -t < 0.2 \text{ GeV}^2$  (top) and  $0.2 < -t < 0.5 \text{ GeV}^2$  (bottom). All plots have  $y$  scale ranging from 0 to 0.05 .

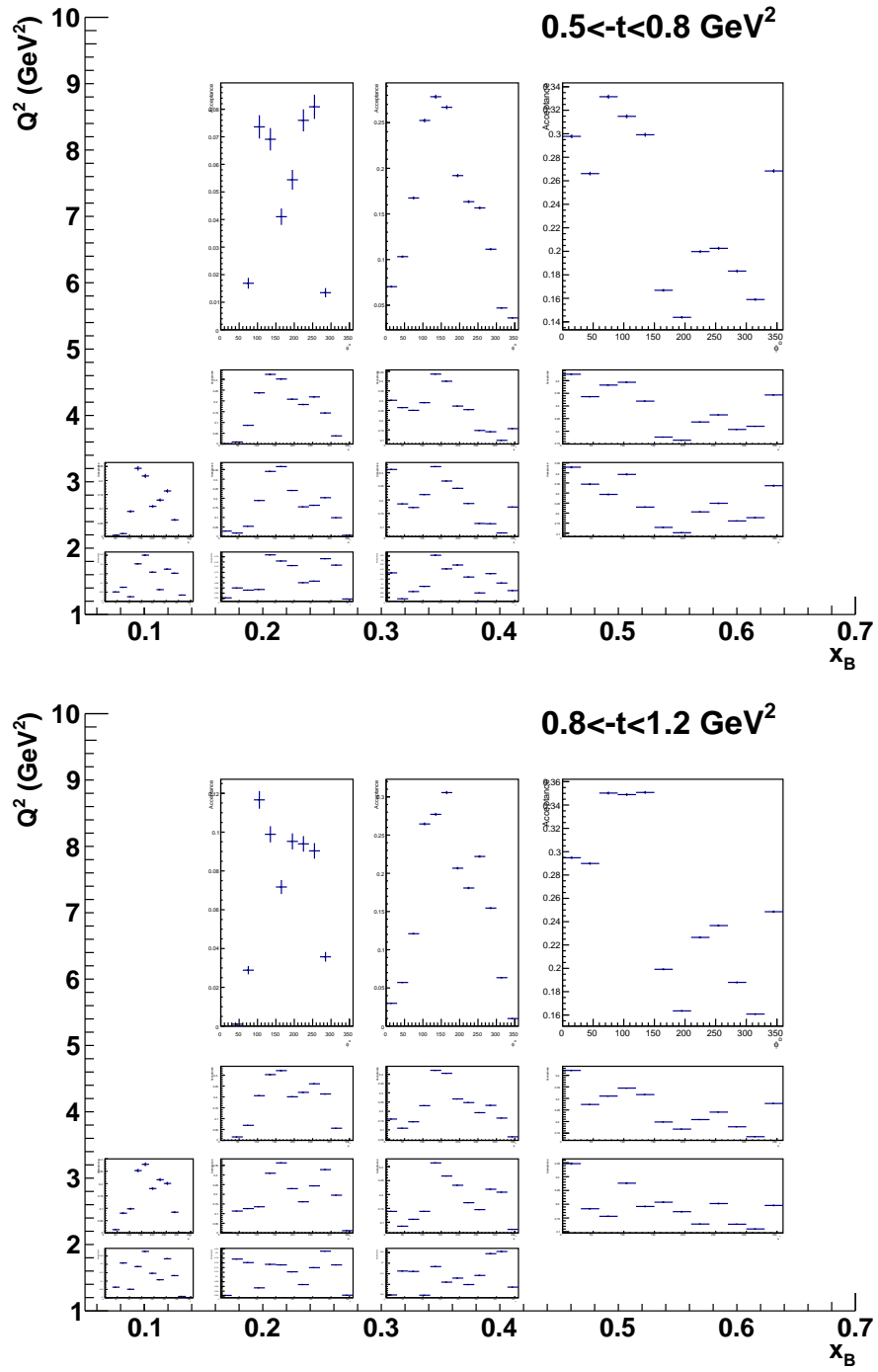


Figure 46: Expected acceptances, including the 10% of efficiency for the CND, for the nDVCS channel:  $0.5 < -t < 0.8 \text{ GeV}^2$  (top) and  $0.8 < -t < 1.2 \text{ GeV}^2$  (bottom). All plots have  $y$  scale ranging from 0 to 0.05.

## References

- [1] D. Müller, D. Robaschik, B. Geyer, F.-M. Dittes, and J. Horejsi, *Fortschr. Phys.* **42** (1994) 101.
- [2] X. Ji, *Phys. Rev. Lett.* **78** (1997) 610; *Phys. Rev. D* **55** (1997) 7114.
- [3] A.V. Radyushkin, *Phys. Lett. B* **380** (1996) 417; *Phys. Rev. D* **56** (1997) 5524.
- [4] J.C. Collins, L. Frankfurt and M. Strikman, *Phys. Rev. D* **56** (1997) 2982.
- [5] K. Goeke, M. V. Polyakov and M. Vanderhaeghen, *Prog. Part. Nucl. Phys.* **47** (2001) 401.
- [6] M. Diehl, *Phys. Rept.* **388** (2003) 41.
- [7] A.V. Belitsky, A.V. Radyushkin, *Phys. Rept.* **418** (2005) 1.
- [8] S. Niccolai, V. Kubarovsky, S. Pisano, and D. Sokhan, JLab experiment E12-11-003.
- [9] A.V. Belitsky, D. Müller, A. Kirchner, *Nucl. Phys. B* **629** (2002) 323-392.
- [10] M. Guidal, *Eur. Phys. J. A* **37** (2008) 319; M. Guidal, H. Moutarde, *Eur. Phys. J. A* **42** (2009) 71.
- [11] M. Guidal, H. Moutarde, M. Vanderhaeghen, *Rep. Prog. Phys.* **76**, 066202 (2013).
- [12] M. Vanderhaeghen, P.A.M. Guichon, M. Guidal, *Phys. Rev. D* **60**, 094017 (1999).
- [13] M. Guidal, M. V. Polyakov, A. V. Radyushkin and M. Vanderhaeghen, *Phys. Rev. D* **72**, 054013 (2005).
- [14] S. Pisano *et al.*, *Phys. Rev.* **D91**, 052014 (2015).
- [15] E. Seder *et al.*, *Phys. Rev. Lett.* **114**, 032001 (2015).
- [16] F.-X. Girod *et al.*, *Phys. Rev. Lett.* **100**, 162002 (2008).
- [17] S. Chen *et al.*, *Phys. Rev. Lett.* **97**, 072002 (2006).
- [18] M. Mazouz *et al.*, *Phys. Rev. Lett.* **99**, 242501 (2007).
- [19] C. Muñoz Camacho *et al.* (Hall-A Collaboration), *Phys. Rev. Lett.* **97**, 262002 (2006).
- [20] S. Stepanyan *et al.* (CLAS Collaboration), *Phys. Rev. Lett.* **87**, 182002 (2001).
- [21] A. Airapetian *et al.* (HERMES Collaboration), *JHEP* **06** **0806**, 066 (2008); A. Airapetian *et al.* (HERMES Collaboration), *JHEP* **06**, 019 (2010).
- [22] H.-S. Jo *et al.*, *Phys. Rev. Lett.* **115**, 212003 (2015).
- [23] C. Hyde-Wright, B. Michel, C. Munoz Camacho and J. Roche, JLab experiment E12-06-114.
- [24] F. Sabatié, A. Biselli, V. Burkert, L. Elouadrhiri, M. Garçon, M. Holtrop, D. Ireland, K. Joo, W. Kim, JLab experiment E12-06-119.
- [25] L. Elouadrhiri, H. Avakian, V. Burkert, M. Guidal, M. Lowry, L. Pappalardo, and S. Procureur, JLab experiment E-12-12-010, conditionally approved.
- [26] C. Munoz Camacho, C. Hyde-Wright, P.-Y. Bertin, JLab experiment E07-007.
- [27] C. Munoz Camacho, R. Parenduyan, T. Horn, JLab experiment E12-13-010.

- [28] C.H. Hyde, P.-Y. Bertin, A. Camsonne, JLab Experiment E08-025.
- [29] Technical Design Report of the CLAS12 Forward Tagger, <http://www.ge.infn.it/~batta/jlab/ft-tdr.2.0.pdf>.
- [30] St. Goertz, W. Meyer, and G. Reichertz, Progress in Particle and Nuclear Physics **49** (2002) 403.
- [31] G.R. Court, D.W. Gifford, P. Harrison, W.G. Heyes, and M.A. Houlden, Nucl. Instr. Meth. **A 324**, 433 (1993).
- [32] G.R. Court, *et al.*, Nucl. Instr. Meth. **A 527**, 253 (2004).
- [33] C. Dulya, *et al.*, Nucl. Instr. and Meth. **A 398** (1997) 109.
- [34] N. D. Kwaltine, PhD thesis, University of Virginia, 2013.
- [35] K. Slifer, “Proceedings of the 12th International Workshop on Polarized Ion Sources, Targets, and Polarimetry”, Upton, NY (2007) 330.
- [36] P. McKee, Nucl. Instr. Meth. **A 526**, 60 (2004).
- [37] R.T. Giles *et al.*, Nucl. Instr. Meth. **A 252**, 41 (1986).
- [38] E. Smith *et al.*, Nucl. Instr. Meth. **A 432**, 265 (1999).
- [39] V. Baturin *et al.*, Nucl. Instr. Meth. **A 562**, 327 (2006).
- [40] M. Ungaro, private communication.
- [41] J.B. Birks, Proc. Phys. Soc. **A64**, 874 (1951).
- [42] D. Sokhan, <http://clasweb.jlab.org/wiki/index.php/Daria> .
- [43] S. Niccolai, [http://clasweb.jlab.org/rungroups/e1-dvcs/wiki/index.php/CLAS12\\_neutron\\_detector:update\\_on\\_simulation](http://clasweb.jlab.org/rungroups/e1-dvcs/wiki/index.php/CLAS12_neutron_detector:update_on_simulation) (September 2008).
- [44] A. El Aloui and E. Voutier, CLAS-NOTE 2009-024.
- [45] H. Avakyan, private communication.
- [46] M. Lacombe *et al.*, Phys. Rev C **21** (1980) 861.
- [47] D. Sokhan, analysis underway.
- [48] P. Bosted <https://www.jlab.org/Hall-B/secure/eg1-dvcs/bosted/Exclusive/exclnote.pdf>.
- [49] R. De Vita, private communication.
- [50] A. Avakian *et al.*, JLab conditionally approved proposal C12-11-111.
- [51] S. Procureur, private communication.
- [52] A.V. Afanasev *et al.*, J. Exp. Theor. Phys. **102**, 220 (2006).
- [53] S. Kuhn, A. Deur, V. Dharmawardane, K. Griffioen, D. Crabb, Y. Prok, T. Forest, Jefferson Lab Experiment E12-06-109.
- [54] <https://www.jlab.org/Hall-B/clas12-web/clas12-expt1.jpg>.